A hypoelastic stress resultant shell approach for simulations of textile composite reinforcement forming

Bo Chen, Julien Colmars, Naim Naouar, Philippe Boisse

Composites: Part A 149 (2021) 106558

Contents lists available at ScienceDirect

Composites Part A

journal homepage: www.elsevier.com/locate/compositesa

A hypoelastic stress resultant shell approach for simulations of textile composite reinforcement forming

Bo Chen, Julien Colmars, Naim Naouar, Philippe Boisse *

Université de Lyon, LaMCoS, CNRS, INSA-Lyon F-69621, France

ARTICLE INFO

Keywords:
A. Fabrics/textiles
C. Process simulation
C. Finite element analysis (FEA)
E. Forming
Stress resultant shells

ABSTRACT

A stress resultant shell approach is proposed to simulate the draping of textile composite reinforcements with continuous fibers. This approach naturally makes it possible to take into account the specificity of the deformation of the fibrous reinforcements by considering independent bending and tension stiffness whereas they are linked in standard shell elements. The stress resultants and stress moments are related to membrane strains and curvatures by rate constitutive equations (hypoelastic laws). The experimental tests required to identify the material properties necessary for these constitutive laws in stress resultants are presented. This approach is implemented in the ABAQUS finite element code and can be used by all users of this software. A set of forming tests showed the effectiveness of the approach through comparisons between simulation and experimental results.

1. Introduction

Continuous fiber-reinforced composites are used in the aeronautical industry to reduce weight thus contributing to obtaining a lower fuel consumption and satisfying high performance standards. They also represent an opportunity in the automotive industry to achieve, through weight reduction, the objectives of new norms in terms of CO_2 emissions. One of the main advantages of using composite materials is that their mechanical properties can be tailored to meet the design requirements of specific applications. However, this advantage comes with a significant manufacturing challenge: there are many manufacturing processes for composites that are often complex. Process simulation is a way to avoid costly trial-and-error development.

The present article concerns how to simulate the forming of continuous fiber composite reinforcements and prepregs (a process often called draping). In Liquid Composite Molding (LCM) processes [1–3], a resin is injected onto the dry reinforcement after it has been formed. In the case of prepregs, the resin is present in the reinforcement during thermoforming but is not cured [4–7]. The presence of the uncured matrix modifies the behavior, but the deformation is mainly controlled by the fibers. The fibrous reinforcements or prepregs can be considered as a continuous medium but with a very specific behavior given the fibrous composition. The continuous medium hypothesis has been validated for numerous cases [8,9], whereas other approaches have been developed that model each fiber of the reinforcement [10–14]. Using the latter to simulate the draping of textile reinforcements is difficult given the very large number of fibers in a composite preform.

The forming of textile reinforcements is challenging. Non-developable geometries are achieved through shear angles that can be large (up to 60°). The fibers are quasi-inextensible. Defects can occur during forming, in particular wrinkling [15–18]. Simulations must determine the deformations and stresses during and after the process, the possible occurrence and development of defects, and the direction and density of fibers in the final part.

The fibrous reinforcements generally have one dimension that is small compared with the other two. This dimension is the thickness which can be very small (thin reinforcements) or more significant (thick reinforcements) but it remains much smaller than the warp and weft dimensions. Consequently, the simulation of fibrous reinforcement forming is generally based on shell modeling. However, standard shell models and shell elements built in finite element software cannot be used to simulate the deformation of textiles. The possible slippage between the fibers leads to specific deformation modes that are presented in Section 2. Classical shell theories (in particular Kirchhoff and Mindlin models) are not relevant. In these classical approaches, the bending stiffness is a function of the membrane stiffness and the thickness which leads to a much too high bending stiffness for fibrous shells.

In order to simulate the deformation of textile shells with a bending

* Corresponding author.
E-mail address: philippe.boisse@insa-lyon.fr (P. Boisse).

https://doi.org/10.1016/j.compositesa.2021.106558
Received 6 May 2021; Received in revised form 9 July 2021; Accepted 9 July 2021
Available online 18 July 2021

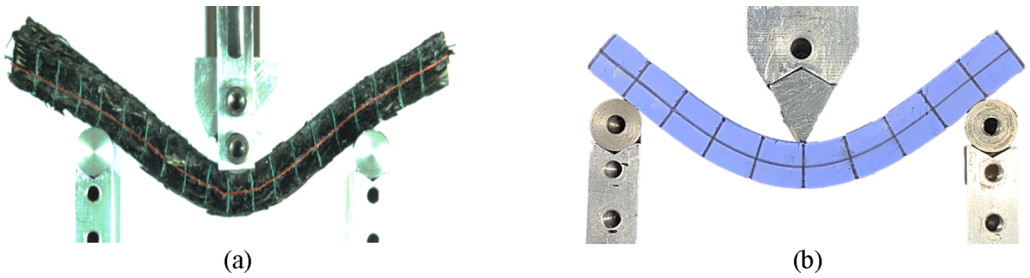

Fig. 1. (a) Bending of a fibrous material. (b) Bending of a classical continuous material. (For interpretation of the references to colour in this figure legend, the reader is referred to the web version of this article.)

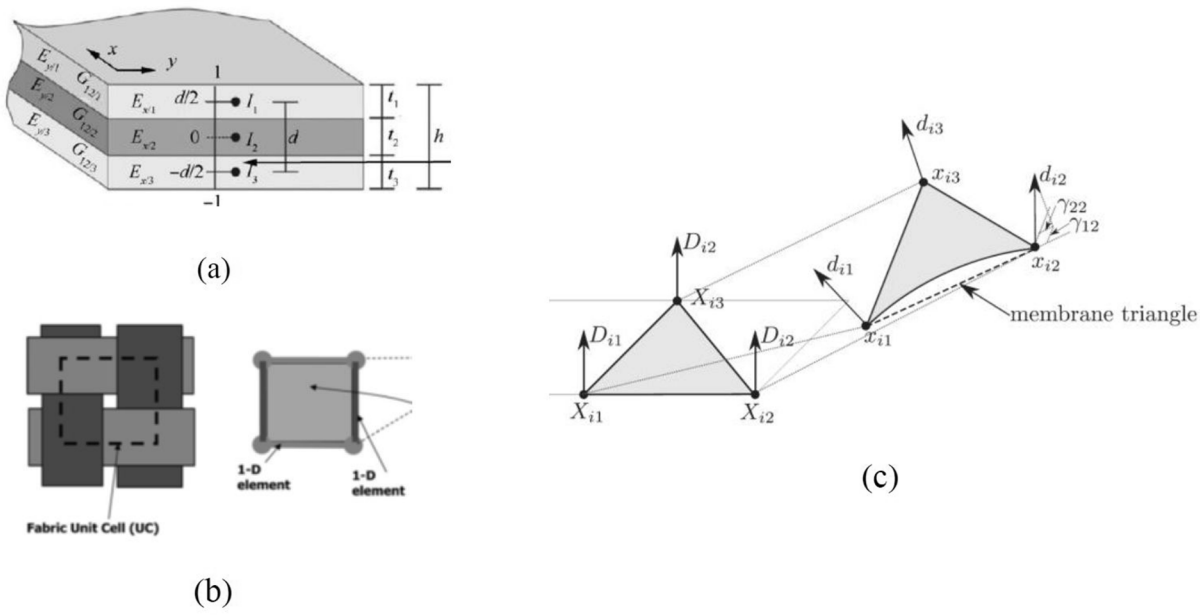

Fig. 2. Different approaches to decouple bending and tension stiffness. (a) The textile reinforcement is considered as a laminate [31]. (b) Modeling by beam and membrane element [37]. (c) Superposition of a membrane and shell element [43].

stiffness corresponding to the effective stiffness of the fabric, different strategies have been proposed. Section 2 presents these approaches which are often somewhat artificial. The objective of this paper is to propose a stress resultant shell approach associated with a hypoelastic behavior for the simulation of the deformation of fibrous reinforcements (Sections 3 and 4). The stress resultant approach is one of the main frameworks in shell and shell finite element formulations [19–21]. It is well suited to take into account the specific bending of textile reinforcements. In the present paper, the shell stress resultant approach was implemented in a user subroutine (Vugens) of the commercial finite element software ABAQUS. It can be used by all users of this code and can also be integrated in other finite element codes.

The experimental tests required to determine the mechanical behavior in terms of stress resultants versus strain are described in Section 5. It is important to have a good understanding of the necessary mechanical tests and their connection with the simulation method in order to envisage the industrial use of such an approach. Section 6 exhibits the validation of the presented approach in cases of combinations of elementary loadings and Section 7 presents a set of forming processes for which the simulations based on the proposed technique were compared with experimental forming. The method was found to be robust and efficient.

2. The specificities of shell approaches for the deformation of composite textile reinforcements

When the structures studied are thin, shell finite element modeling is much more efficient than 3D finite element modeling. In particular, the majority of sheet metal forming simulations are based on shell finite elements [22,23]. When it comes to composite materials, forming is carried out on dry fabrics (without resin) in the case of LCM processes or prepregs where the resin is uncured (in the case of thermoset prepregs) or above the melting temperature (in the case of thermoplastic prepregs). In these different cases, slippage between the fibers may occur which strongly modifies the physics of the deformation and make the bending stiffness much lower than for conventional continuous materials. The weakness of the bending stiffness has in some studies led to the modeling of textile reinforcements forming by membrane approaches, i.e., neglecting the bending stiffness [24–30].

The bending stiffness, albeit low, will condition the onset and the development of possible wrinkles during a forming process [17,31–34]. Fig. 1a shows the deformation of a fibrous reinforcement in 3-point bending (here a 15-mm thick interlock woven fabric [35]) and Fig. 1b shows the deformation in 3-point bending of a classical continuous material (here a 15-mm thick silica gel). In the latter case the bending deformation follows Kirchhoff's theory and the directions initially perpendicular to the mean plane remain perpendicular to the midsurface after deformation. This does not occur during bending deformation

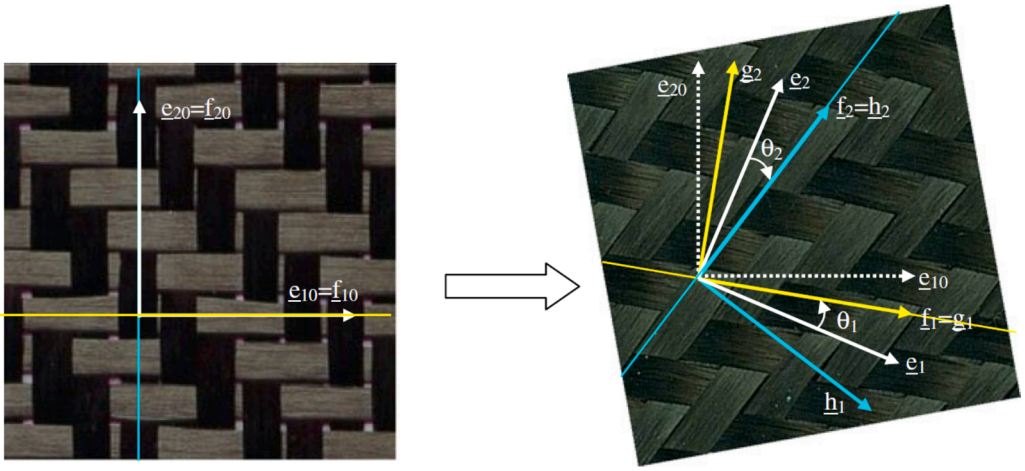

Fig. 3. Orthonormal frames in the fiber direction and the Green Naghdi frame. (For interpretation of the references to colour in this figure legend, the reader is referred to the web version of this article.)

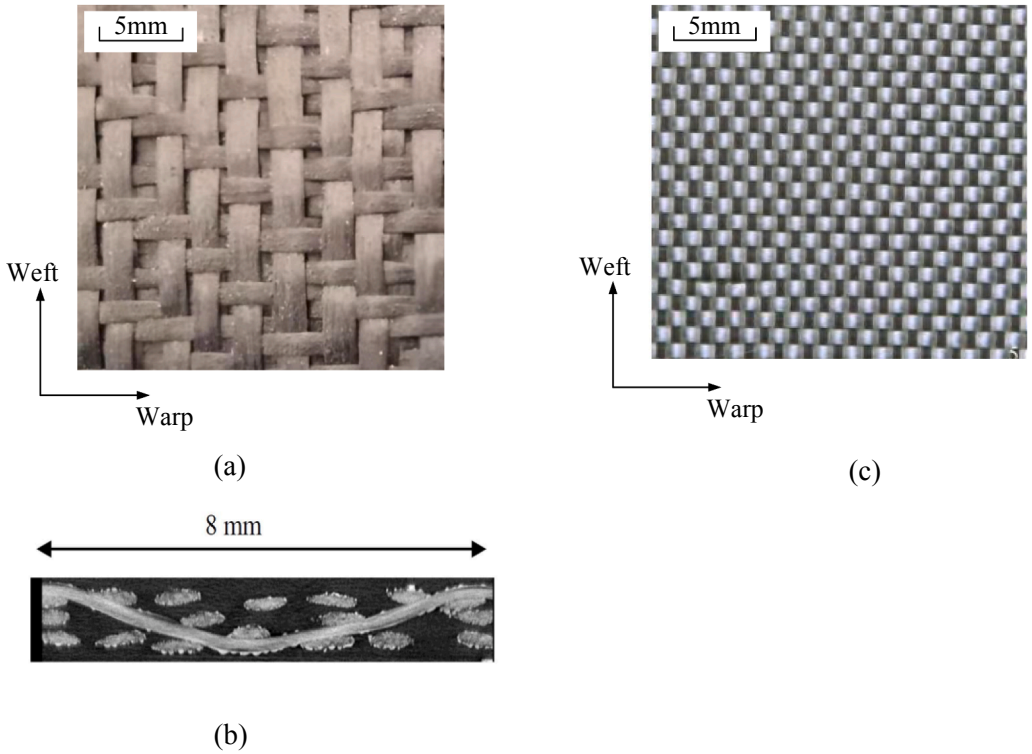

Fig. 4. (a) Interlock G1151 fabric. (b) X-ray Tomography of G1511 fabric [66]. (c) Plain weave fabric.

Table 1
Geometric characteristics of the two types of fabric material.

Material	G1151 fabric	Plain weave
Manufacturer	Hexcel	Hexcel
Fibers	Carbon 6 K	Glass EC9 68
Areal density	630 g/m^2	160 g/m^2
Single layer thickness	1.3 mm	0.14 mm
Yarn density	Warp: 7.5 yarns/cm Weft: 7.4 yarns/cm	Warp: 11.8 yarns/cm Weft: 10.7 yarns/cm

of a fibrous medium. In such a case, the fibers can slip and the material's normal position is fixed by the inextensibility of the fibers and does not remain perpendicular to the surface (Fig. 1a). This results in a much lower bending stiffness of fibrous materials as opposed to continuous materials.

For classical continuous materials following Kirchhoff's law, the tensile stiffness and the thickness determine the bending stiffness. This is not the case for fibrous materials and shells, wherefore shell finite elements based on classical theories cannot be used. To overcome this difficulty and carry out draping simulations of textile reinforcements taking into account the bending rigidity, several methods have been proposed. A first approach involves considering the textile reinforcement as a laminate composed of layers of materials with different Young moduli (Fig. 2a). It is possible to fix the characteristics of the different layers to achieve both the required membrane stiffness and bending stiffness [31,36].

Another method consists in associating finite beam elements in the direction of the warp and weft yarns (to model bending) and membrane elements (to model tension and in-plane shear) (Fig. 2b) [37–40]. The

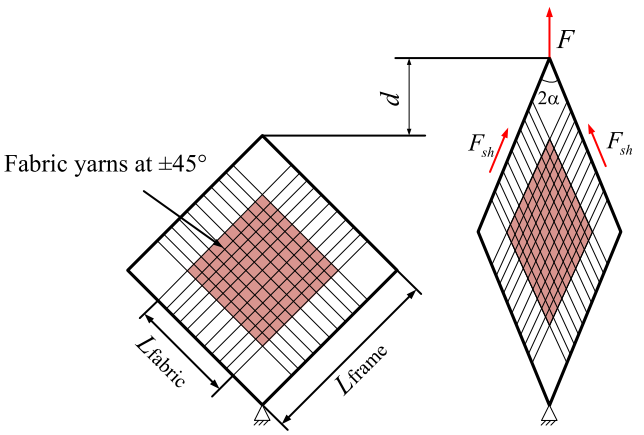

Fig. 5. Schematic diagram of picture frame test. (For interpretation of the references to colour in this figure legend, the reader is referred to the web version of this article.)

Table 2
Principal mechanical properties of the two fabric materials.

Mechanical properties	G1151 fabric	Plain weave
In plane shear ($\gamma = 2\varepsilon_{12}$)	$K_0 = 0.088$ N/mm	$K_0 = 0.411$ N/mm
$dN_{12} = C_{12}d\gamma$	$K_1 = -0.828$ N/mm	$K_1 = -1.110$ N/mm
$C_{12} = K_0 + K_1\lvert\gamma\rvert + K_2\lvert\gamma\rvert^2 +$	$K_2 = 2.924$ N/mm	$K_2 = 5.566$ N/mm
$K_3\lvert\gamma\rvert^3 + K_4\lvert\gamma\rvert^4$	$K_3 = -4.008$ N/mm	$K_3 = -18.711$ N/mm
	$K_4 = 2.031$ N/mm	$K_4 = 19.501$ N/mm
Out of plane bending	$D_{11} = 7.45$ N mm	$D_{11} = 0.5$ N mm
$dM_{11} = D_{11}d\chi_{11}$	$D_{22} = 7.45$ N mm	$D_{22} = 0.5$ N mm
$dM_{22} = D_{22}d\chi_{22}$		
Tensile stiffness	$C_{11} = 21500$ N/mm	$C_{11} = 1150$ N/mm
$dN_{11} = C_{11}d\varepsilon_{11}$	$C_{22} = 21500$ N/mm	$C_{22} = 1150$ N/mm
$dN_{22} = C_{22}d\varepsilon_{22}$		
Coulomb friction coefficient		
Ply to ply	0.21	
Ply to mold	0.23	

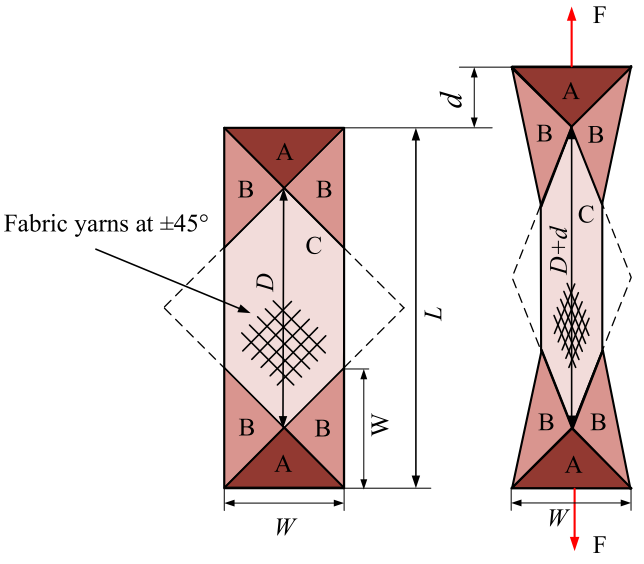

Fig. 6. Schematic diagram of bias extension test. (For interpretation of the references to colour in this figure legend, the reader is referred to the web version of this article.)

superimposition of membrane and shell finite elements with only bending stiffness is also an option (Fig. 2c) [34,41–43]. In the latter approach, the material properties must be different in the membrane

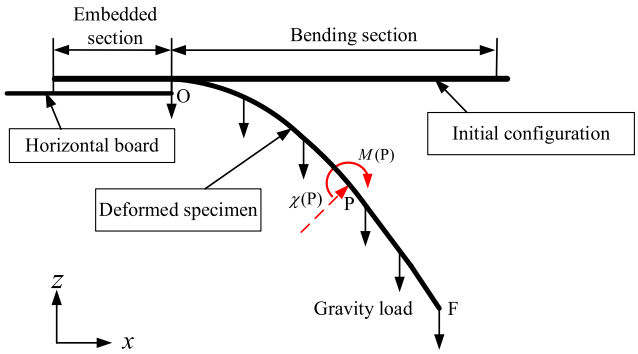

Fig. 7. Schematic diagram of bending test. (For interpretation of the references to colour in this figure legend, the reader is referred to the web version of this article.)

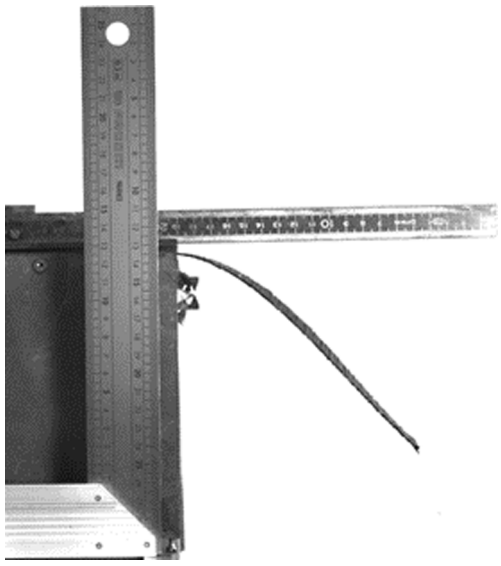

Fig. 8. Bending experiment test. (For interpretation of the references to colour in this figure legend, the reader is referred to the web version of this article.)

and shell elements. While they may be effective with respect to the deformation of the midsurface of the textile reinforcement, these methods are somewhat artificial and are not based on the physics of bending of fibrous materials. An alternative method is the stress resultant shell approach, which is presented below. As you will see, we propose a stress resultant shell approach based on a hypoelastic constitutive equation developed within the commercial finite element software ABAQUS.

3. Stress resultant shells

Computational shell analyses are dominated by the so-called continuum-based shell approach which consists in imposing shell kinematic assumptions in a three-dimensional finite element [44–46]. Stress resultant shells constitute an alternative [19–21].

The virtual work equation links internal virtual work δW_{int}, external virtual work δW_{ext} and acceleration virtual work δW_{acc}:

$$\delta W_{\text{ext}} - \delta W_{int} = \delta W_{\text{acc}} \tag{1}$$

for any virtual displacement equal to zero on the imposed displacement boundary part. In the case of a stress resultant shell, the internal virtual work takes the following form:

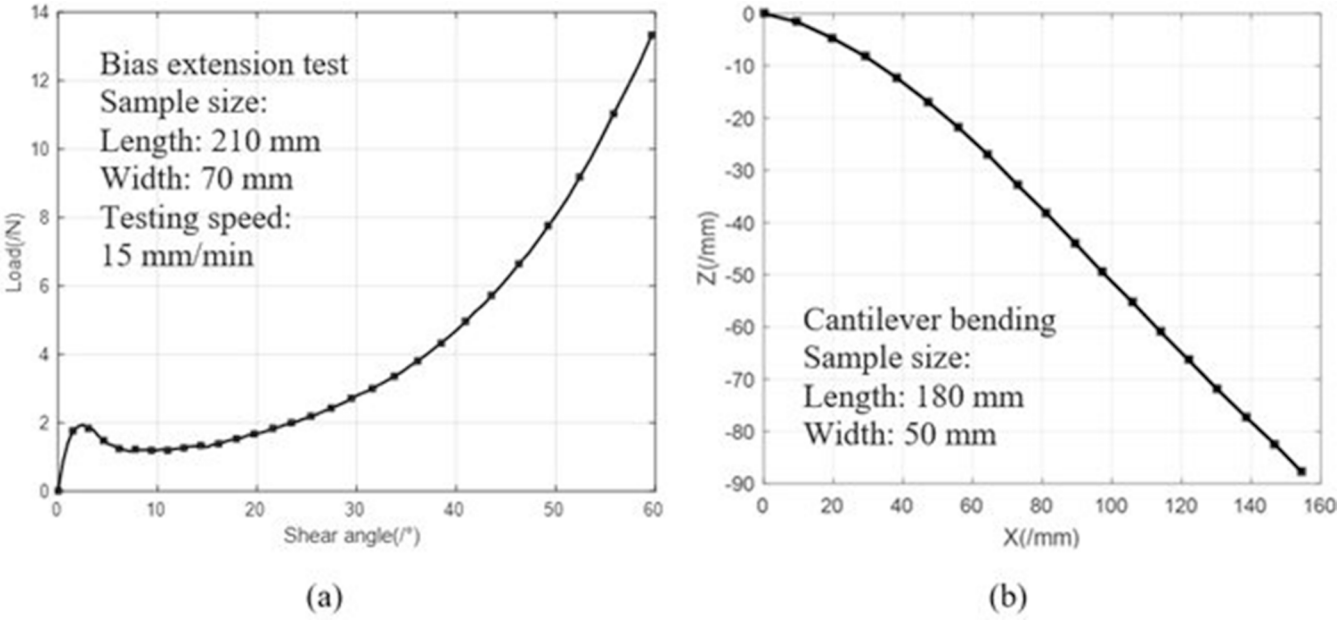

Fig. 9. Testing G1151 properties. (a) Bias extension test curve. (b) Cantilever bending curve. (For interpretation of the references to colour in this figure legend, the reader is referred to the web version of this article.)

$$\delta W_{int} = \int_A \delta\varepsilon_{11}N^{11} + \delta\varepsilon_{22}N^{22} + \delta\varepsilon_{12}N^{12} + \delta\chi_{11}M^{11} + \delta\chi_{22}M^{22} + \delta\chi_{12}M^{12}dA \tag{2}$$

where A is the midsurface of the shell, $\delta\varepsilon_{11}, \delta\varepsilon_{22}$ are the virtual axial strains in the warp and weft directions,$\delta\varepsilon_{12}$ is the virtual in-plane shear strain, $\delta\chi_{11}, \delta\chi_{22}, \delta\chi_{12}$ are the virtual curvatures in these directions. N^{11}, N^{22}, N^{12} are the stress resultants and M^{11}, M^{22}, M^{12} are the stress moments (or stress couples) with:

$$N^{\alpha\beta} = \int_{-\frac{h}{2}}^{\frac{h}{2}} \sigma^{\alpha\beta}dz \qquad M^{\alpha\beta} = \int_{-\frac{h}{2}}^{\frac{h}{2}} z\sigma^{\alpha\beta}dz \tag{3}$$

Here, the indices $\alpha,\ \beta$ belong to the set (1, 2), $\sigma^{\alpha\beta}$ are the components of the Cauchy stress. The stress resultants $N^{\alpha\beta}$ are energy conjugates to the membrane strains $\varepsilon_{\alpha\beta}$ and the stress moments $M^{\alpha\beta}$ are energy conjugates to the curvatures $\chi_{\alpha\beta}$. The constitutive laws considered in the presented approach are relations between resultant stresses $N^{\alpha\beta}$ and membrane strains $\varepsilon_{\alpha\beta}$ (membrane behavior) and between stress moments $M^{\alpha\beta}$ and curvatures $\chi_{\alpha\beta}$ (bending behavior). Membrane and bending behaviors occur independently which is well adapted to the modeling of textile reinforcements. Moreover, membrane and bending stiffnesses can be determined experimentally and taken into account independently.

In the present work, the behavior laws are rate constitutive equations (hypoelastic models). They relate the stress resultant rates to the membrane strain rates and the stress moment rates to the curvature rates. The simulations described in this paper are performed within the ABAQUS/explicit code and based on the Vugens user subroutine. In this subroutine, the stress resultants are calculated from membrane deformations and curvatures.

A semi-discrete shell finite element approach that falls within the framework of stress resultant shells has been proposed in an in-house F. E. code [47]. This approach considers a finite element as a sum of mesoscopic woven unit cells. It is a rotation free approach; the curvatures are computed from the position of the neighboring elements. A viscoelastic simulation of the deformation of UD tapes has been performed in ABAQUS [42] by superimposing built-in membrane finite elements and shell finite elements using a Ugens subroutine considering only the bending behavior.

4. Rate constitutive equations

Rate constitutive equations (or hypoelastic laws) are widely employed to simulate large deformations of solids [48–50] and in particular the large deformations of fibrous materials [51–55]. They are much utilized in finite element codes and in user subroutines. For large deformations of materials and in particular of composite textile reinforcements, hypoelastic laws are an alternative to the use of hyperelastic models [56–59]. In the case of stress resultant shells, the objective is to calculate the stress resultants at time t_{n+1} from their values at t_n and the strain and curvature increments. Rate constitutive equations for stress resultants and stress moments (or stress couples) are considered:

$$\mathbf{N}^{\nabla} = \mathbf{C} : \dot{\boldsymbol{\varepsilon}} \qquad \mathbf{M}^{\nabla} = \mathbf{D} : \dot{\boldsymbol{\chi}} \tag{4}$$

Here, $\dot{\boldsymbol{\varepsilon}}$ and $\dot{\boldsymbol{\chi}}$ are the time derivatives of the membrane strain and curvature tensors, $\mathbf{C}$ and $\mathbf{D}$ are the membrane and bending constitutive tensors, and $\mathbf{N}^{\nabla}$ and $\mathbf{M}^{\nabla}$ are the objective derivatives of the stress resultant and stress moment. The objective derivative is the time derivative for an observer fixed to the material. The aim is that no stress is created by the rigid rotations. There are several objective derivatives. In the case of the rotational objective derivatives, which are the most used thanks to their simplicity, the time derivative is made in a rotated frame. The most classical rotation derivatives are those of Jaumann (derivative in the co-rotational frame) [60] and of Green Naghdi (derivative in the basis rotated by the polar rotation) [61]. In the case of fibrous media, it has been shown that the appropriate rotation for the objective derivative is that of the fiber [62,63]. The approach presented below concerns a material with two directions of fibers as is the case for a majority of composite textile reinforcements and in particular the woven reinforcements considered in this paper.

In the user subroutines of the ABAQUS/explicit code, the input and output quantities are expressed on the Green Naghdi basis ($\mathbf{e_1}$, $\mathbf{e_2}$) which is obtained during deformation by the polar rotation $\mathbf{R}$, defined by the polar decomposition of the deformation gradient $\mathbf{F} = \mathbf{RU}$.

$$\mathbf{e}_1 = \mathbf{R}.\ \mathbf{e}_1^0 \qquad \mathbf{e}_2 = \mathbf{R}.\ \mathbf{e}_2^0 \tag{5}$$

The initial orthogonal basis $(\mathbf{e}_1^0, \mathbf{e}_2^0)$ coincides with the initial directions of the warp and weft fibers $(\mathbf{f}_1^0, \mathbf{f}_2^0)$ (Fig. 3). Fiber directions are given by the deformation gradient during deformation.

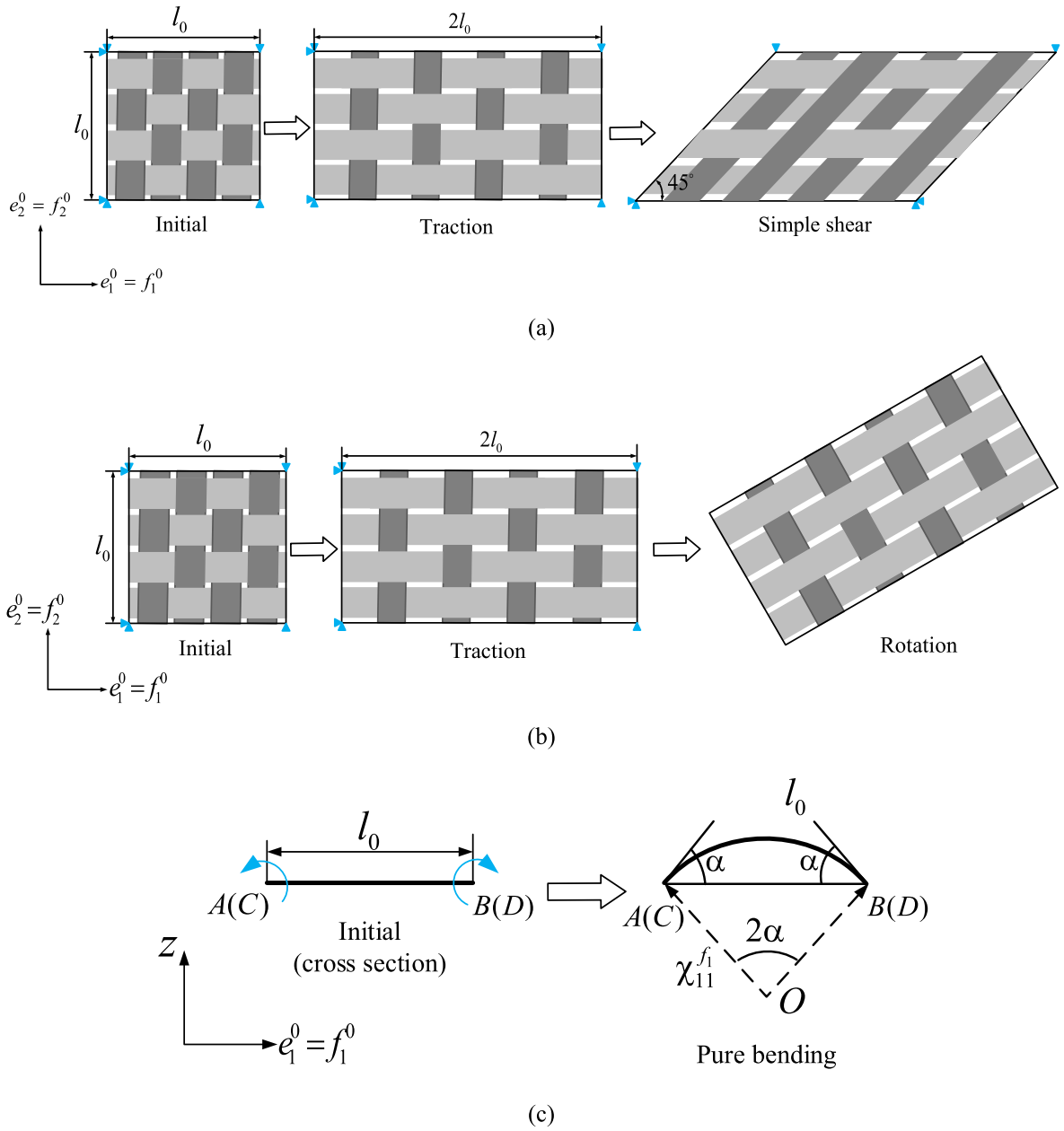

Fig. 10. Three elementary tests. (a) 45° simple shear test after a traction ratio 2.(b) Rigid body rotation test after a traction ratio 2. (c) pure bending test. (For interpretation of the references to colour in this figure legend, the reader is referred to the web version of this article.)

$$\mathbf{f}_1 = \frac{\mathbf{F}\cdot\mathbf{f}_1^0}{\|\mathbf{F}\cdot\mathbf{f}_1^0\|} \qquad \mathbf{f}_2 = \frac{\mathbf{F}\cdot\mathbf{f}_2^0}{\|\mathbf{F}\cdot\mathbf{f}_2^0\|} \tag{6}$$

Two orthonormal bases are defined from the direction of the fibers: one basis directed by the warp fiber direction g($\mathbf{g}_1$, $\mathbf{g}_2$) with $\mathbf{g}_1 = \mathbf{f}_1$ and the other directed by the weft fiber direction h($\mathbf{h_1}$, $\mathbf{h_2}$) with $\mathbf{h_2} = \mathbf{f_2}$ (Fig. 3). For the time increment [t_n, t_{n+1}], the components of the membrane deformation increment and the curvature increment are given on the Green Naghdi basis:

$$\mathbf{d\varepsilon} = d\varepsilon_{\alpha\beta}^{GN}\,\mathbf{e}_\alpha \otimes \mathbf{e}_\beta \qquad \mathbf{d\chi} = d\chi_{\alpha\beta}^{GN}\,\mathbf{e}_\alpha \otimes \mathbf{e}_\beta \tag{7}$$

The components of the two tensors on the bases g and h are deduced from:

$$\begin{aligned} d\varepsilon_{11}^g &= \mathbf{g}_1\cdot\mathbf{d\varepsilon}\cdot\mathbf{g}_1 & d\varepsilon_{12}^g &= \mathbf{g}_1\cdot\mathbf{d\varepsilon}\cdot\mathbf{g}_2 \\ d\chi_{11}^g &= \mathbf{g}_1\cdot\mathbf{d\chi}\cdot\mathbf{g}_1 & d\chi_{12}^g &= \mathbf{g}_1\cdot\mathbf{d\chi}\cdot\mathbf{g}_2 \\ d\varepsilon_{22}^h &= \mathbf{h_2}\cdot\mathbf{d\varepsilon}\cdot\mathbf{h_2} & d\varepsilon_{12}^h &= \mathbf{h_1}\cdot\mathbf{d\varepsilon}\cdot\mathbf{h_2} \\ d\chi_{22}^h &= \mathbf{h_2}\cdot\mathbf{d\chi}\cdot\mathbf{h_2} & d\chi_{12}^h &= \mathbf{h_1}\cdot\mathbf{d\chi}\cdot\mathbf{h_2} \end{aligned} \tag{8}$$

These increments of membrane deformations and curvatures are used to calculate the components of stress resultant increments on the g and h bases.

$$\begin{aligned} dN_{11}^g &= C_{11}d\varepsilon_{11}^g & dN_{12}^g &= C_{12}d\varepsilon_{12}^g & dM_{11}^g &= D_{11}d\chi_{11}^g & dM_{12}^g &= D_{12}d\chi_{11}^g \\ dN_{22}^h &= C_{22}d\varepsilon_{22}^h & dN_{12}^h &= C_{12}d\varepsilon_{12}^h & dM_{22}^h &= D_{22}d\chi_{22}^h & dM_{12}^h &= D_{12}d\chi_{12}^h \end{aligned} \tag{9}$$

Here, C_{11}, C_{22} are the tensile stiffness in the warp and weft directions, C_{12} is the in-plane shear stiffness, D_{11}, D_{22} are the bending stiffness in the warp and weft directions and D_{12} it is the cross term of bending stiffness. These stiffnesses are not necessarily constant: especially C_{12} depends on the in-plane shear. The stress resultants are cumulated over the time

Table 3
Theoretical value of the elementary test.

		Strain output	Stress resultant output
Simple shear test after the traction	First step	$\boldsymbol{\varepsilon}^f = \begin{bmatrix}\varepsilon_{11}\\ \varepsilon_{22}\\ \varepsilon_{12}\end{bmatrix}^f = \begin{bmatrix}0.693\\ 0\\ 0\end{bmatrix}$	$\mathbf{N}^f = \begin{bmatrix}N_{11}\\ N_{22}\\ N_{12}\end{bmatrix}^f = \begin{bmatrix}693\\ 0\\ 0\end{bmatrix}$
	Second step	$\boldsymbol{\varepsilon}^f = \begin{bmatrix}\varepsilon_{11}\\ \varepsilon_{22}\\ \varepsilon_{12}\end{bmatrix}^f = \begin{bmatrix}0.693\\ 0.347\\ 0.785\end{bmatrix}$	$\mathbf{N}^f = \begin{bmatrix}N_{11}\\ N_{22}\\ N_{12}\end{bmatrix}^f = \begin{bmatrix}693\\ 347\\ 0\end{bmatrix}$
Rigid body rotation test after the traction	First step	$\boldsymbol{\varepsilon}^f = \begin{bmatrix}\varepsilon_{11}\\ \varepsilon_{22}\\ \varepsilon_{12}\end{bmatrix}^f = \begin{bmatrix}0.693\\ 0\\ 0\end{bmatrix}$	$\mathbf{N}^f = \begin{bmatrix}N_{11}\\ N_{22}\\ N_{12}\end{bmatrix}^f = \begin{bmatrix}693\\ 0\\ 0\end{bmatrix}$
	Second step	$\boldsymbol{\varepsilon}^f = \begin{bmatrix}\varepsilon_{11}\\ \varepsilon_{22}\\ \varepsilon_{12}\end{bmatrix}^f = \begin{bmatrix}0.693\\ 0\\ 0\end{bmatrix}$	$\mathbf{N}^f = \begin{bmatrix}N_{11}\\ N_{22}\\ N_{12}\end{bmatrix}^f = \begin{bmatrix}693\\ 0\\ 0\end{bmatrix}$
Pure bending		$\boldsymbol{\chi}^f = \begin{bmatrix}\chi_{11}\\ \chi_{22}\\ \chi_{12}\end{bmatrix}^f = \begin{bmatrix}1\\ 0\\ 0\end{bmatrix}$	$\mathbf{M}^f = \begin{bmatrix}M_{11}\\ M_{22}\\ M_{12}\end{bmatrix}^f = \begin{bmatrix}10\\ 0\\ 0\end{bmatrix}$

increment $[t_n, t_{n+1}]$ following the Hughes and Winget scheme [48,63].

$$\begin{aligned}
(N^g_{11})^{n+1} &= (N^g_{11})^n + (dN^g_{11})^{n+1/2} \quad (N^g_{12})^{n+1} = (N^g_{12})^n + (dN^g_{12})^{n+1/2}\\
(M^g_{11})^{n+1} &= (M^g_{11})^n + (dM^g_{11})^{n+1/2} \quad (M^g_{12})^{n+1} = (M^g_{12})^n + (dM^g_{12})^{n+1/2}\\
\left(N^h_{22}\right)^{n+1} &= \left(N^h_{22}\right)^n + \left(dN^h_{22}\right)^{n+1/2} \quad \left(N^h_{12}\right)^{n+1} = \left(N^h_{12}\right)^n + \left(dN^h_{12}\right)^{n+1/2}\\
\left(M^h_{22}\right)^{n+1} &= \left(M^h_{22}\right)^n + \left(dM^h_{22}\right)^{n+1/2} \quad \left(M^h_{12}\right)^{n+1} = \left(M^h_{12}\right)^n + \left(dM^h_{12}\right)^{n+1/2}
\end{aligned} \tag{10}$$

The stress resultants at time t_{n+1} are obtained by adding those in the two warp and weft directions:

$$\begin{aligned}
(\mathbf{N})^{n+1} &= (\mathbf{N}^g)^{n+1} + \left(\mathbf{N}^h\right)^{n+1}\\
(\mathbf{M})^{n+1} &= (\mathbf{M}^g)^{n+1} + \left(\mathbf{M}^h\right)^{n+1}
\end{aligned} \tag{11}$$

The output of the Vugens subroutine consists of the components of the stress resultants on the Green Naghdi basis which are now determined at the end of the increment (n + 1 index is omitted, all the quantities are at t_{n+1}).

$$\begin{aligned}
N^e_{\alpha\beta} &= N^g_{11}(\mathbf{e}_\alpha.\mathbf{g}_1)(\mathbf{e}_\beta.\mathbf{g}_1) + N^h_{22}(\mathbf{e}_\alpha.\mathbf{h}_2)(\mathbf{e}_\beta.\mathbf{h}_2)\\
&\quad + N^g_{12}(\mathbf{e}_\alpha.\mathbf{g}_1)(\mathbf{e}_\beta.\mathbf{g}_2) + N^h_{12}(\mathbf{e}_\alpha.\mathbf{h}_1)(\mathbf{e}_\beta.\mathbf{h}_2)\\
M^e_{\alpha\beta} &= M^g_{11}(\mathbf{e}_\alpha.\mathbf{g}_1)(\mathbf{e}_\beta.\mathbf{g}_1) + M^h_{22}(\mathbf{e}_\alpha.\mathbf{h}_2)(\mathbf{e}_\beta.\mathbf{h}_2)\\
&\quad + M^g_{12}(\mathbf{e}_\alpha.\mathbf{g}_1)(\mathbf{e}_\beta.\mathbf{g}_2) + M^h_{12}(\mathbf{e}_\alpha.\mathbf{h}_1)(\mathbf{e}_\beta.\mathbf{h}_2)
\end{aligned} \tag{12}$$

Note: the moment components M^g_{12} and M^h_{12} are neglected in the following, which assumes that the bending stiffness of the woven reinforcement is given by that of the yarns in the warp direction as well as the weft direction. This assumption is also made since there are no or few measures of cross bending stiffness.

Remark: The membrane stiffness (relating stress results to membrane deformations) and the bending stiffness (relating stress moments to curvatures) are coupled in classical approaches based on the Kirchhoff assumption where the normal remains perpendicular to the mean surface. In the present approach, Eq. (9) uses independent membrane and bending stiffnesses. This makes it possible to consider a low bending stiffness in the case of shells composed of fibers.

5. Identification of mechanical characteristics

5.1. Material description

The fabric analyzed in the present work was the G1151® carbon reinforcement manufactured by Hexcel [64,65]. It is presented in Fig. 4a and b. A glass plain weave fabric was also considered in Section 7.2 (Fig. 4c). The geometric parameters of the textile reinforcements are presented in Table 1. The methods to characterize the hypoelastic behavior during in-plane shear, bending and tensile behavior are given in this section below.

5.2. In-plane shear behavior

The textile material in-plane shear behavior can be determined by the picture frame test and bias extension test [67–70]. The shear angle which is defined as the angle change between the weft and warp yarn directions can be easily observed and measured. The relationship between the shear angle increment $d\gamma$ and shear strain increment $d\varepsilon_{12}$ is:

$$d\gamma = 2d\varepsilon_{12} \tag{13}$$

5.2.1. Picture frame

As shown in Fig. 5, the woven fabric is clamped within an initially square picture frame at each side. The picture frame deforms into a rhombus under the machine load applied on the opposite corner nodes, causing the material within the frame to be theoretically subjected to a uniform pure shear deformation [67,68,71,72]. When the relative displacement of the nodes of the opposite corners is d (Fig. 5), the shear angle γ is:

$$\gamma = \frac{\pi}{2} - 2\alpha = \frac{\pi}{2} - 2cos^{-1}\left(\frac{\sqrt{2}L_{\text{frame}} + d}{2L_{\text{frame}}}\right) \tag{14}$$

where L_{frame} is the side length of the picture frame, and α is half the angle between the adjacent sides of the picture frame. The stress resultant N_{12} (N/mm) is related to the load on the frame F which is measured in this test:

$$N_{12} = \frac{F_{sh}}{L_{\text{fabric}}} = \frac{F}{2L_{\text{fabric}}cos\alpha} = \frac{F}{2L_{\text{fabric}}cos\ \left(\frac{\pi}{4} - \frac{\gamma}{2}\right)} \tag{15}$$

Here, L_{fabric} is the side length of the material in the experiment.

The measurement of F as a function of the shear angle γ gives the experimental curve $N_{12}(\gamma)$, which is approximated by a polynomial. By taking the derivative of this polynomial, the shear stiffness C_{12} of the rate shear equation that is used in the approach described in Section 4 (Eq. (9)) is obtained as (Table 2):

$$\begin{aligned}
dN_{12} &= C_{12}d\gamma \quad (\gamma = 2\varepsilon_{12})\\
C_{12} &= K_0 + K_1|\gamma| + K_2|\gamma|^2 + K_3|\gamma|^3 + K_4|\gamma|^4
\end{aligned} \tag{16}$$

5.2.2. Bias extension test

The bias extension test is another alternative approach to measure the in-plane shear behavior of a woven material. As shown in Fig. 6, a rectangular specimen was clamped in both ends, and the material's two yarn directions were at +45° of the machine load direction. The specimen was stretched from its initial length L to $L + d$. In this process, based on the quasi-inextensibility of the fibers, there were three different shear zones. Zone A had no shear angle, and the shear angle in zone B was half that of zone C. The theoretical shear angle γ in zone C

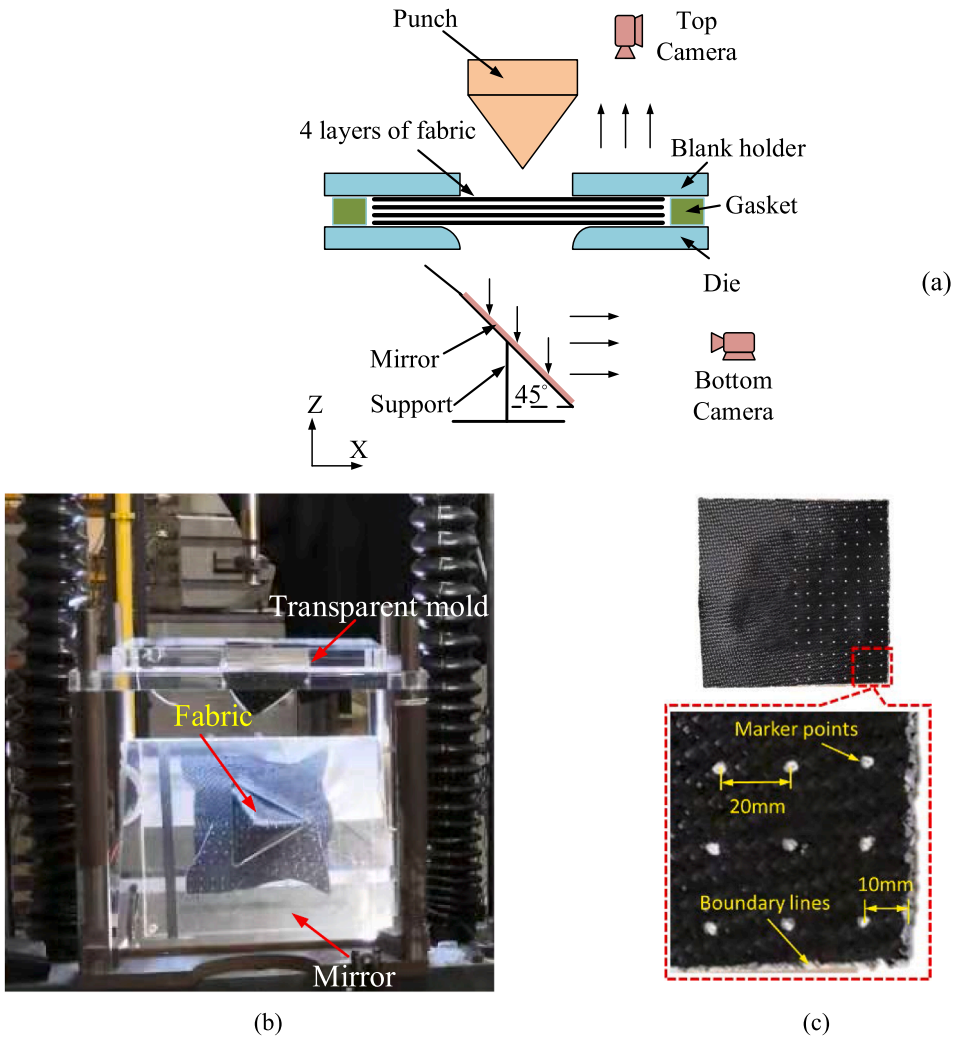

Fig. 11. (a) Schematic diagram of the forming experiment. (b) Experiment device. (c) Marker points on the fabric. (For interpretation of the references to colour in this figure legend, the reader is referred to the web version of this article.)

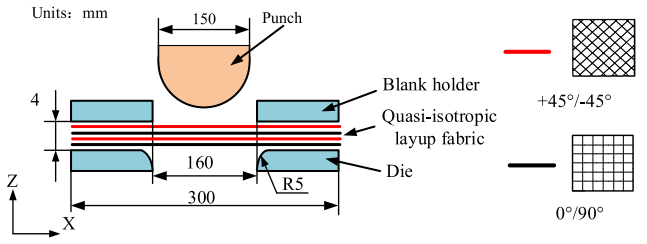

Fig. 12. Hemisphere forming geometry parameters. (For interpretation of the references to colour in this figure legend, the reader is referred to the web version of this article.)

can be calculated according to the geometry relationship:

$$\gamma = \frac{\pi}{2} - 2cos^{-1}\left(\frac{D+d}{\sqrt{2}D}\right) \tag{17}$$

A shear moment on a unit area M_s of the woven material is defined to describe the internal load of the material shear. This shear moment is related to the force on the specimen F based on the energy conservation [69,70,73].

The resultant shear force N_{12} is related to the shear moment M_s:

$$M_s = N_{12}cos\gamma \tag{18}$$

The measure of the load F gives the shear stress-resultant N_{12} as a function of the shear angle γ:

$$N_{12}(\gamma) = \frac{1}{(2L-3W)cos\gamma}\left(\left(\frac{L}{W}-1\right)F\left(cos\frac{\gamma}{2}-sin\frac{\gamma}{2}\right) - WN_{12}\left(\frac{\gamma}{2}\right)cos\frac{\gamma}{2}\right) \tag{19}$$

In the same way as for the picture frame test, this curve $N_{12}(\gamma)$ is approximated by a polynomial. By taking the derivative of this polynomial, the shear stiffness C_{12} is obtained as $dN_{12} = C_{12}d\gamma$ (Eq. (16) and Table 2):

5.3. Bending behavior

The material bending behavior can be determined by the cantilever bending test [33,74–79]. In the cantilever test, the specimen is bent under gravity (Fig. 7). By obtaining the profile of the deformed midline, it can be utilized to calculate the bending stiffness. A rectangular specimen was used in which the yarn direction was parallel to the sides of the specimen, one end of the specimen was fixed and the other end was free. An example of the cantilever bending experiment is shown in Fig. 8.

The deformed midline of the specimen is determined by an optical method and this curve is approximated by an analytical curve (for instance, quartic B-splines in [80]). The analytical form of the curve provides the curvature of the deformed midline $\chi_{\alpha\alpha}$ at any point. The weight of the specimen fixes the bending moment $M_{\alpha\alpha}$ for all points of

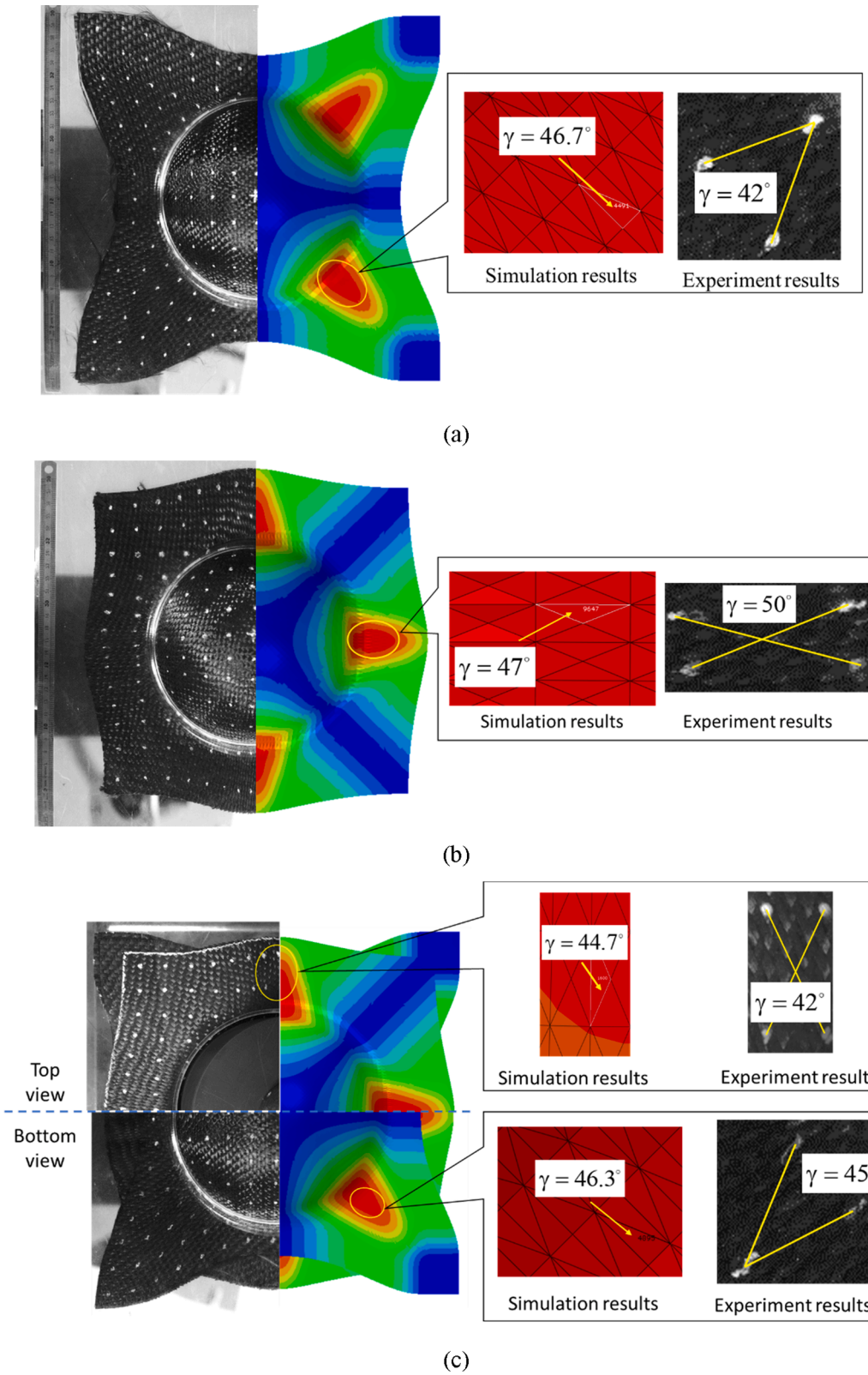

Fig. 13. Experiments and simulations of hemispherical forming deformed fabric and shear angle comparison. (a) Single layer of 0°/90°. (b) Single layer of ± 45°. (c) Four layers of quasi-isotropic layer-up. (For interpretation of the references to colour in this figure legend, the reader is referred to the web version of this article.)

the specimen and the bending behavior curve $M_{\alpha\alpha}$ ($\chi_{\alpha\alpha}$) is determined in this way. This experimental determination is made in both the warp and weft directions ($\alpha = 1,2$), and by taking the derivative of $M_{11}(\chi_{11})$ and M_{22} (χ_{22}), the bending stiffnesses D_{11} and D_{22} of the rate bending equations that are used in the approach described in Section 4 can be obtained as (Table 2):

$$dM_{11} = D_{11}\, d\chi_{11} \qquad dM_{22} = D_{22}\, d\chi_{22} \tag{20}$$

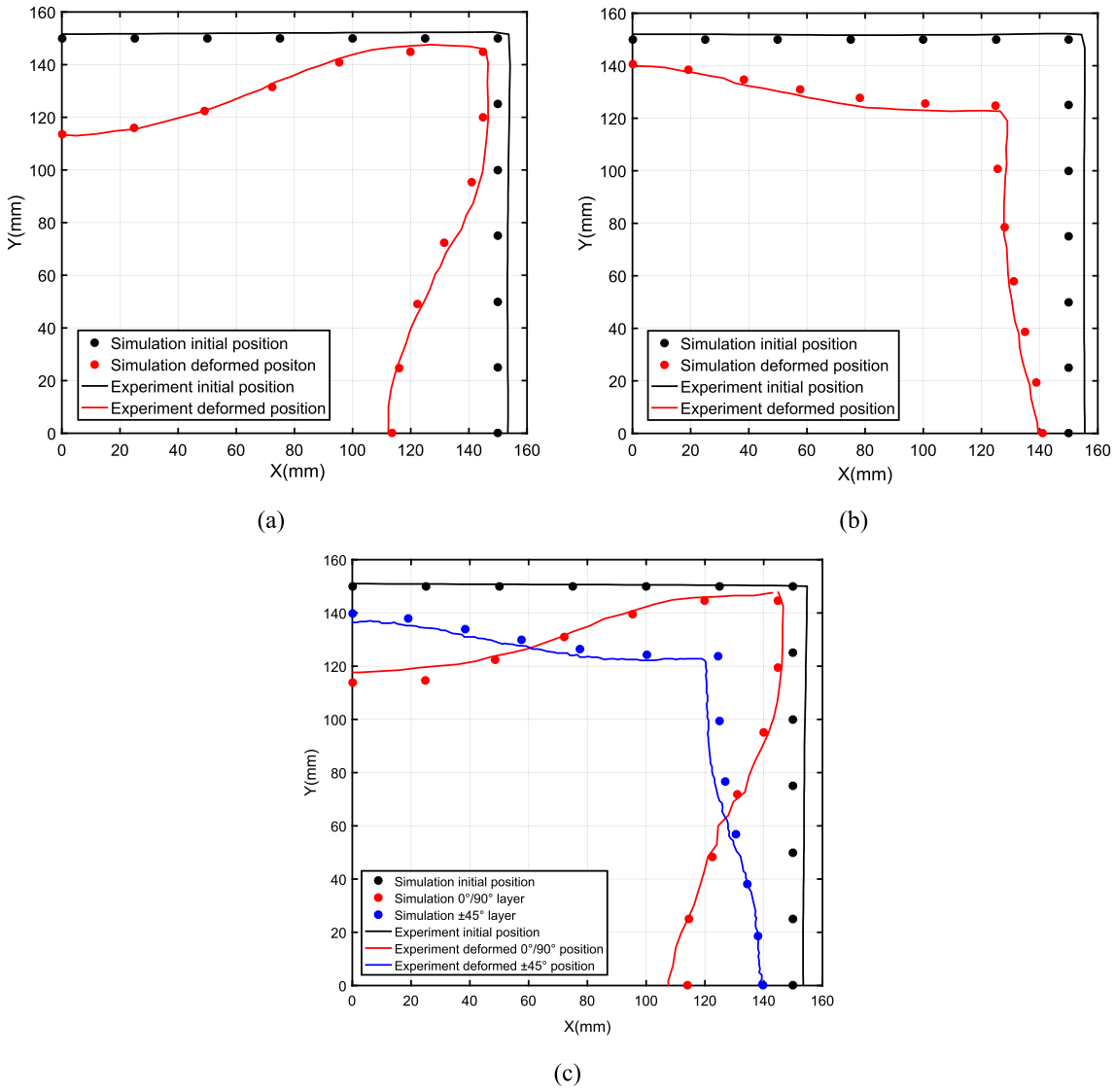

Fig. 14. Hemispherical forming fabric contour comparison between simulation and experiments. (a) Single layer of 0°/90°. (b) Single layer of ±45°. (c) Four-layer quasi-isotropic layup. (For interpretation of the references to colour in this figure legend, the reader is referred to the web version of this article.)

In the present work, as is common to do and often well verified in practice, the bending stiffnesses were assumed to be constant with respect to curvature.

5.4. Tensile behavior

The tensile behavior of a woven material can be determined by uniaxial or biaxial tensile tests. A biaxial test is necessary to consider the coupling of the tensile behavior in the warp and weft directions due to the weaving [81–84]. However, this coupling does not play a major role during forming of a textile reinforcement such as the G1151 which is considered in this paper. The tensile stiffnesses C_{11} and C_{22} in the warp and weft directions were assumed to be constant (Table 2). They are calculated from the number of fibers in the warp and weft yarn of the G1151 fabric and the stiffness of a single fiber.

$$dN_{11} = C_{11}\, d\varepsilon_{11} \qquad dN_{22} = C_{22}\, d\varepsilon_{22} \tag{21}$$

5.5. The tested material properties

Although some work has indicated that there are couplings between the different behaviors of the textile reinforcements [85–89], these couplings were not taken into account in the present work. This assumption was made both for simplicity and because of a lack of experimental data regarding this point for most of the textile reinforcements. For the contact properties, Coulomb friction coefficients were assumed as constant in the forming process. The mechanical properties of the two fabric materials used in this work are presented in Table 2. Fig. 9 shows the testing results curves for the G1151 fabric in in-plane shear (bias extension test) and bending (cantilever test). The sample size and testing speeds are given in Fig. 9.

6. Elementary tests

Elementary tests were performed to show that the calculation was correct at the element level by comparison to theoretical results. A single four-node shell element was selected to conduct the analyses. As shown in Fig. 10, the initial element geometry was a square with an initial length l_0, the yarn directions were parallel to the element edges. Three types of elementary tests, listed below, were carried out and compared with the theoretical result.

(a) 45° simple shear test after the traction along the yarn direction f_1(Fig. 10a).

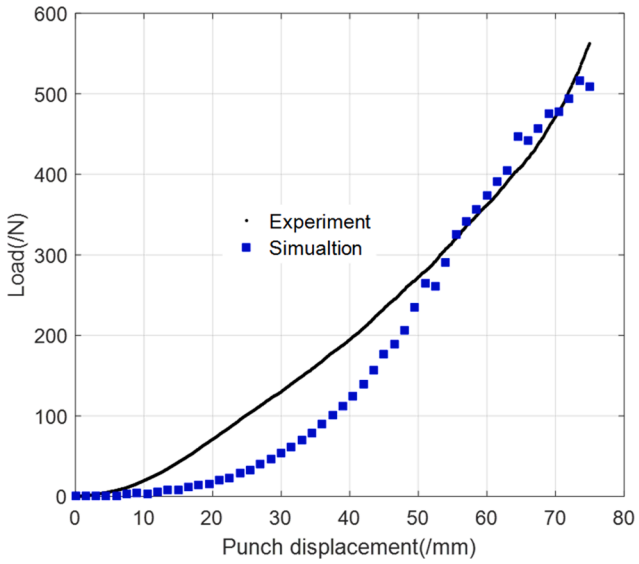

Fig. 15. Draping force during the hemispherical forming of a four-layer quasi-isotropic stack. Comparison of experimental and numerical force. (For interpretation of the references to colour in this figure legend, the reader is referred to the web version of this article.)

(b) Rigid body rotation test after the traction along the yarn direction f_1 (Fig. 10b).
(c) Pure bending test (Fig. 10c).

In elementary tests (a) and (b), the tensile stiffness in the two yarn directions was $C_{11} = C_{22} = 1000$ (N/mm), and the other material stiffnesses were equal to zero. In the elementary test (c), the membrane stiffness was identical to that in the prior two element tests and the bending stiffness D_{11} along the yarn direction f_1 was 10 N mm. The theoretical output values of the strain and the stress resultants for the three types of elementary tests are listed in Table 3.

The elementary tests (a) and (b) were two-step simulations. In the first step of these two elementary tests, they generated the strain and the resultant force only along the yarn direction f_1. In the second step of test (a), the element was subjected to a stretch deformation in the yarn direction f_2 while the deformation in the yarn direction f_1 remained unchanged. The objective of this step was to show that the deformation in one fiber direction did not affect the other. In the second step of test (b), the element was subjected to a rigid body rotation, and the strain and resultant force were supposed to remain unchanged which would show the objectivity of the computation (the rigid body rotation should not lead to spurious stress resultants).

The elementary test (c) was a single-step simulation. The two edges AC and BD of the element were subjected to a rotation, thus the element should have a uniform bending along the yarn direction f_1, and the rotation angle was set as $\alpha = \frac{1}{2l_0}$. The objective of this test (c) was to show that the bending moment would be obtained according to the yarn curvature and the introduced hypoelastic laws, thus indicating that the element's bending behavior was well decoupled from that of the membrane.

These three elementary simulation tests were performed using the presented stress resultant shell approach, and the numerical simulations gave rise to the expected theoretical results in all cases.

7. Forming simulations and experimental comparison

The objective of the proposed approach was to simulate the forming of textile composite reinforcements. To examine the relevance of the presented hypoelastic stress resultant shell approach, forming experiments were carried out and compared with simulations performed by the proposed method. The forming experiments are done on a single ply or simultaneously on a stack of several plies.

7.1. Experimental setup

The experiments presented below were implemented on a ZwichRoell 100KN traction machine. The TestXpertII software was used to control the movement's speed (set at 30 mm/min for all the types of shape forming) and distance. As shown in Fig. 11b, the blank holder and the die mold were made of poly (methyl methacrylate) (PMMA), which is transparent, in order to observe the material deformation during the forming process, and they were fixed during the forming process. In Fig. 11a, two cameras were placed at the material top side and bottom side respectively, through the reflection of the mirror, pictures were recorded with imaging software. Marker points were painted on the fabric at equal intervals as shown in Fig. 11c, and the marker-based tracking approach was adopted to obtain the deformation at different locations. The forming experiments were performed at room temperature.

7.2. Hemispherical forming

Fig. 12 shows the hemispherical forming parameters. The initial dimension of the fabric was 300 mm × 300 mm, the fabric material used for the experiment was G1151®, and the material geometry description is presented in Section 5.1. Three material lay-up configurations were assumed to include either a single layer or multi-layers. For the single layer, the material configurations in 0°/90° and ±45° were done separately. For the multi-layers, the four-layer stack with a quasi-isotropic lay-up was done as shown in Fig. 12 (2x[0°–90°, +45°/−45°), and the final punch displacement in the hemispherical forming was 75 mm.

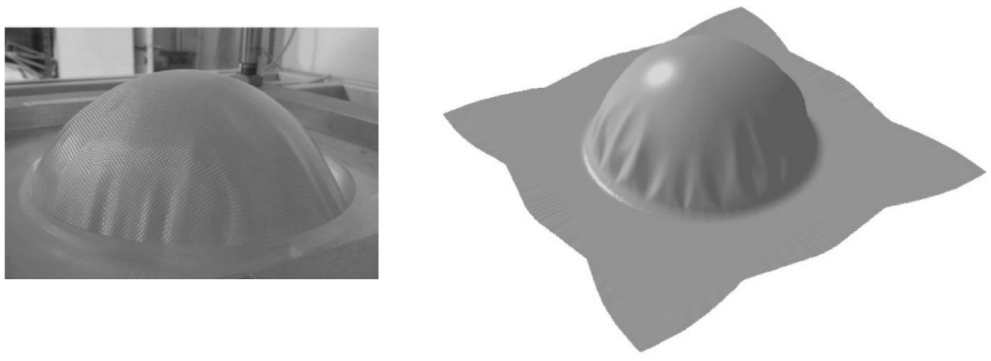

(a) (b)

Fig. 16. Hemispherical forming of four layers quasi-isotropic plain weave. (a) Experiment result [90]. (b) Simulation result.

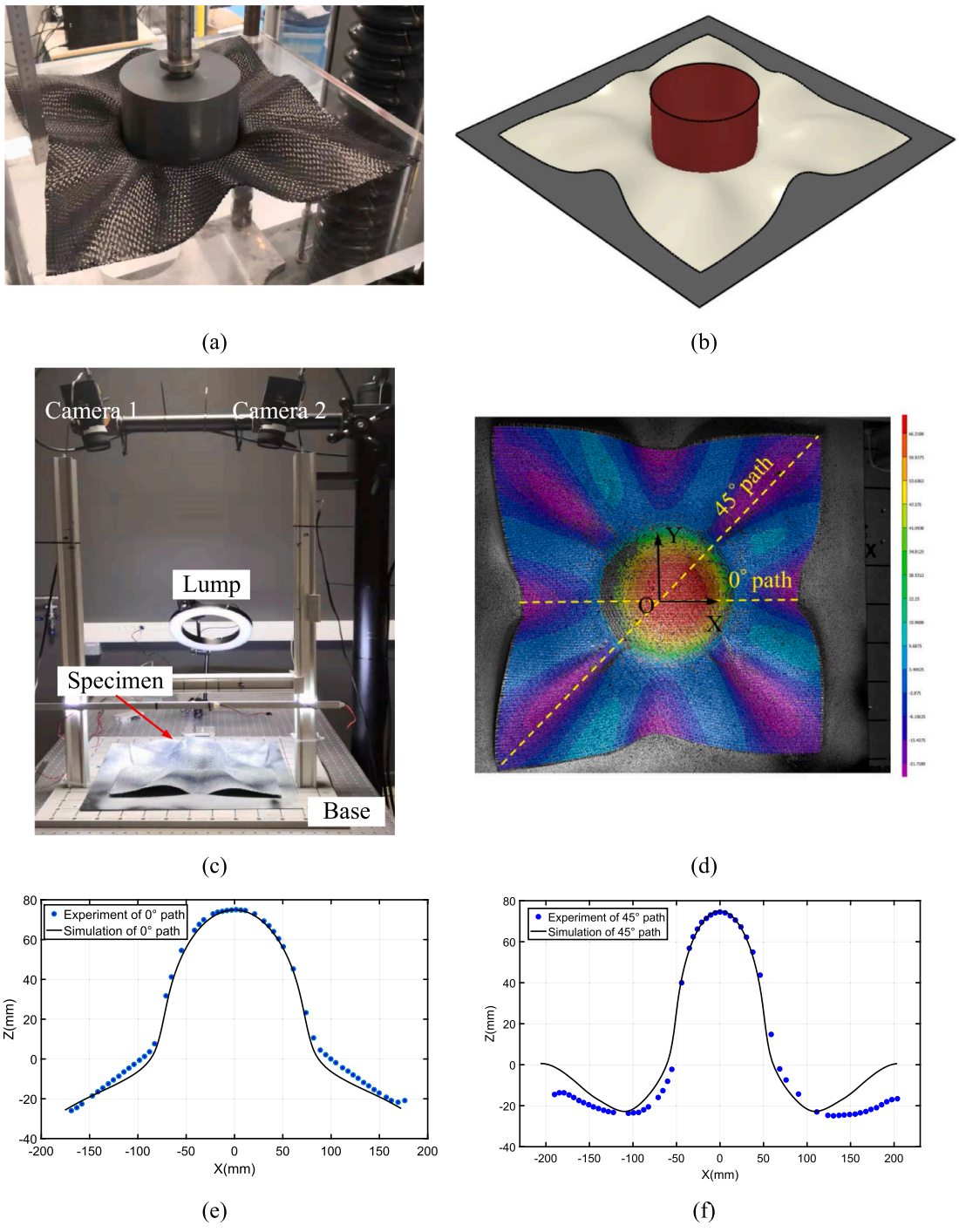

Fig. 17. Hemispherical forming without a blank holder. (a) Final deformed shape from the experiment. (b) Final deformed shape from the simulation. (c) DIC experiment settings (d) DIC result of the final deformed shape. (e) Comparison between simulation and experiment along the 0° path (f) Comparison between simulation and experiment along the 45° path. (For interpretation of the references to colour in this figure legend, the reader is referred to the web version of this article.)

The final deformed experimental shapes are presented on the left side of Fig. 13. Fig. 13a exhibits the forming of a single layer of 0°/90°, Fig. 13b shows the forming of a single layer of ±45°, and Fig. 13c presents the forming of a stack of four layers with a quasi-isotropic layup. Given the use of a blank holder, but also in view of the mechanical characteristics of the G1151 reinforcement, none of them exhibited wrinkles in the deformed textile reinforcements.

The simulations corresponding to experiments were executed according to the following. Three node shell elements were used to mesh each fabric layer, the forming simulation was performed over one quarter of the fabric, and 10,000 elements were used for each layer. The mechanical properties of the textile reinforcement required as input for the stress resultant shell approach simulation are presented in Table 2.

7.2.1. *In-plane shear angle comparison*

Because the properties of a manufactured composite part depend highly on the yarn directions, it is important for the simulation model to correctly predict the in-plane shear angles. The comparison of the in-plane shear angle between experiment and simulation is shown on the right side of Fig. 13. The in-plane shear angles were measured in the

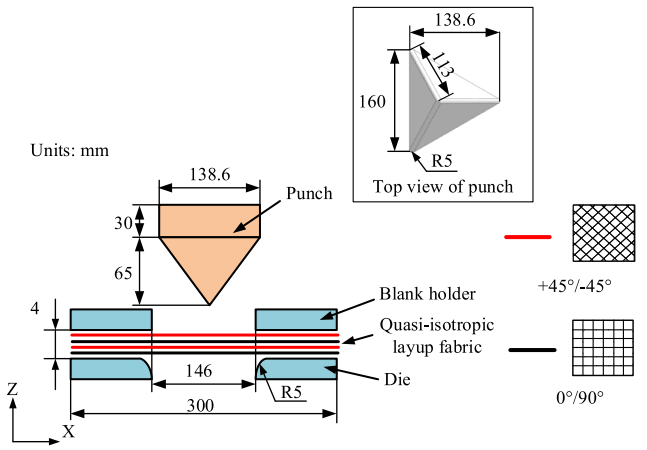

Fig. 18. Settings for the tetrahedral forming geometry. (For interpretation of the references to colour in this figure legend, the reader is referred to the web version of this article.)

experiments with the help of marker points. As can be seen in Fig. 13, the measured in-plane shear angles were in good agreement with those calculated by simulations.

7.2.2. Fabric contour comparison

The deformed fabric contour takes on the final shape of the preform, and the experimental fabric contour can be extracted through an imaging process. Fabric contour comparisons of the hemispherical forming are shown in Fig. 14. The black and red lines represent respectively the initial and deformed position of the fabric in the experiment and the black and red dots represent respectively the initial and deformed positions of the fabric in the simulation. According to these comparisons, the deformed fabric profile obtained by experiment and simulation were in good agreement.

7.2.3. Draping force-displacement

The draping force is shown in Fig. 15 in the case of the hemispherical forming of the four-layer quasi-isotropic stack as a function of the punch displacement. The experimental and numerical loads are in correct agreement for the highest values of the forming forces. For the lower

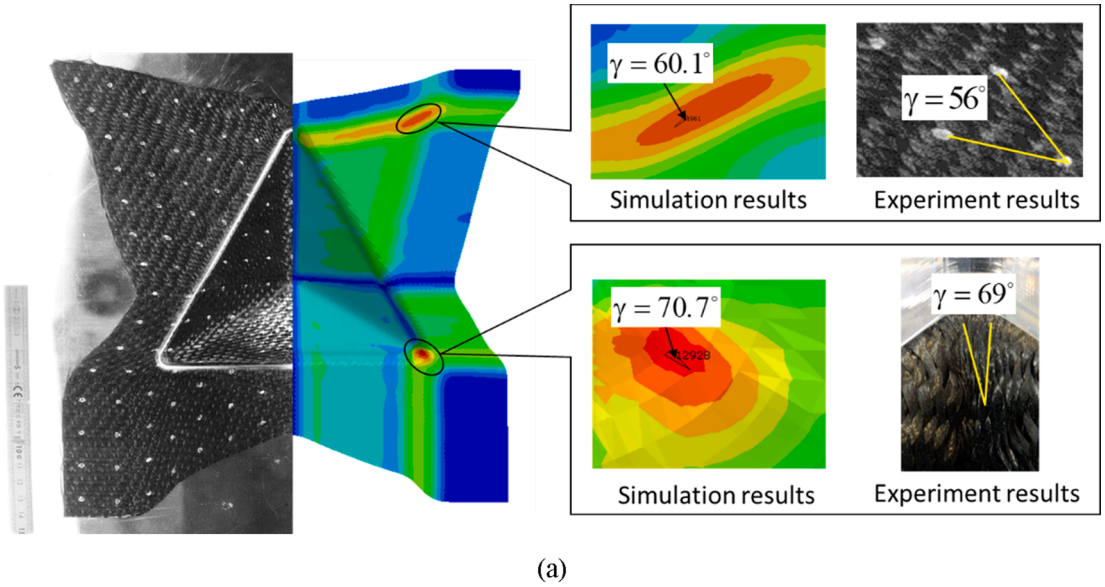

Fig. 19. Tetrahedral single layer deformed fabric and shear angle comparison. (a) Single layer of 0°/90°. (b) Single layer of ±45°. (For interpretation of the references to colour in this figure legend, the reader is referred to the web version of this article.)

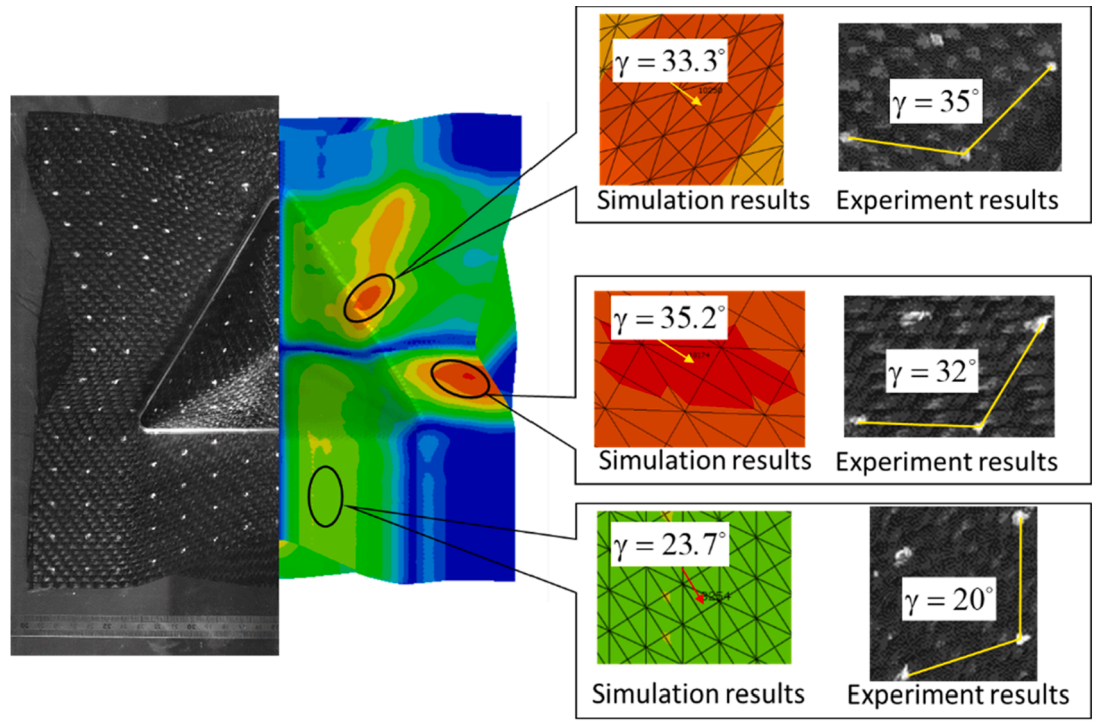

(a)

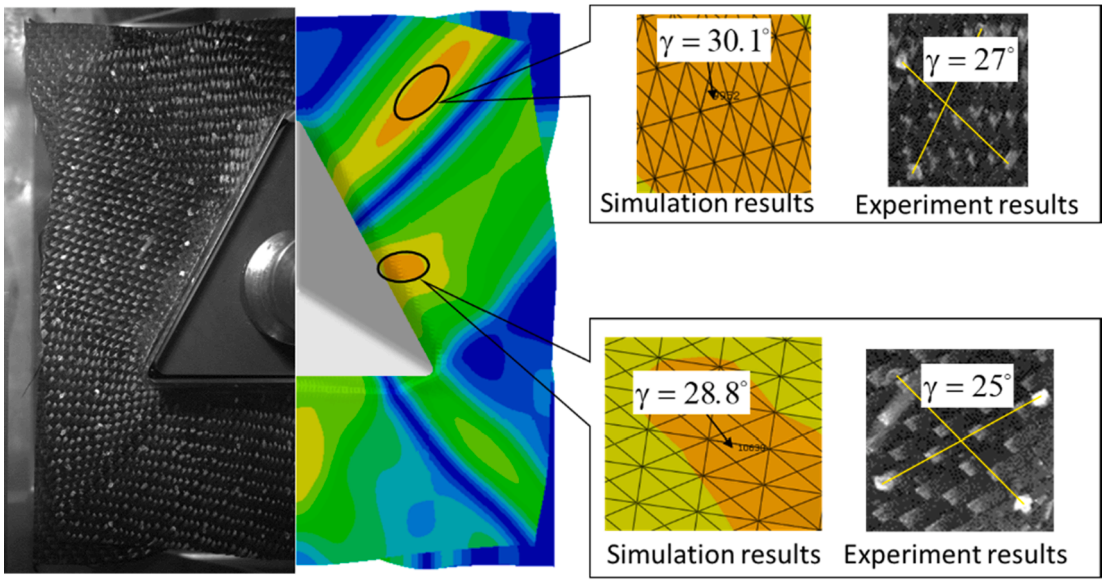

(b)

Fig. 20. Tetrahedral deformed fabric of four-layer quasi-isotropic layup and shear angle comparison. Bottom view. (b) Top view. (For interpretation of the references to colour in this figure legend, the reader is referred to the web version of this article.)

forces at the beginning of the draping process, the experimental force on the punch are higher than those obtained by simulation. This may be related to some friction in the forming system.

7.2.4. Wrinkling during forming of multilayered reinforcements

Wrinkling is one of the major defects that can take place during forming. During forming of multilayer fabric with different orientations, the deformation is different for the two adjacent layers with varying orientation, causing slippage between layers. If this slippage is restricted due to the interlayer friction, it may generate compressive forces in the yarn direction which will cause wrinkling between the contact layers [90].

The material used in the experiment presented in Fig. 16a was the plain weave fabric (Fig. 4c), whose material properties are given in Table 2. The experimental geometry parameters are shown in Fig. 12. Wrinkles appeared during forming of the four-layer stack with the quasi-isotropic layup forming experiment as shown in Fig. 16a. The corresponding simulations were carried out using the presented stress

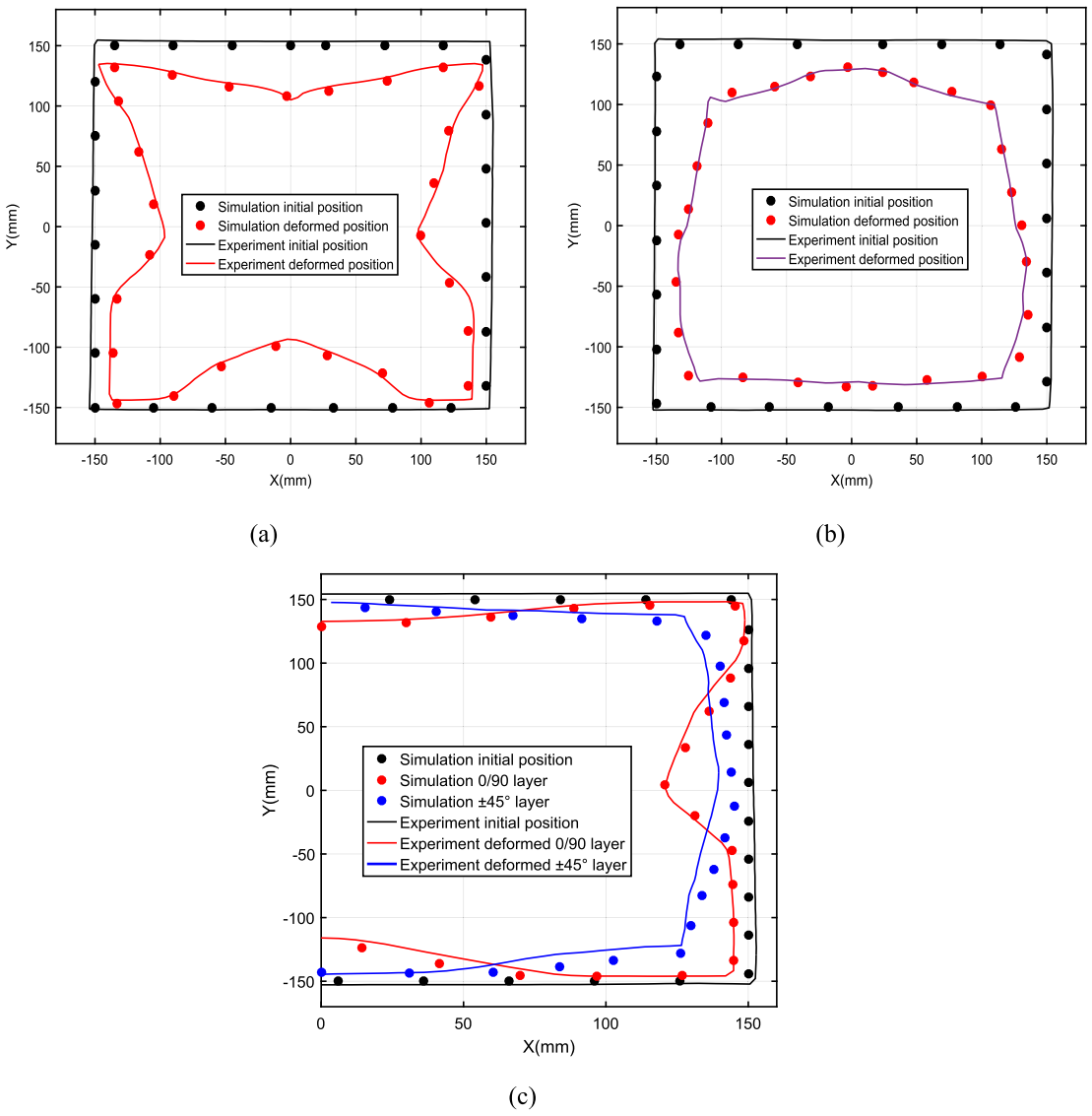

Fig. 21. Comparison of fabric profile from tetrahedral forming obtained by simulation and experiments. (a) Single layer of 0°/90°. (b) Single layer of ±45°. (c) Four-layer quasi-isotropic layup. (For interpretation of the references to colour in this figure legend, the reader is referred to the web version of this article.)

resultant shell approach and a comparison between simulation and experimental results is shown in Fig. 16b. In the case of the plain weave stack with a quasi-isotropic layup, significant wrinkles in the hemispherical zone were obtained in the simulation. For the hemispherical forming of four layers with a quasi-isotropic layup of the G1151 fabric, no wrinkles were observed in the experiments due to the different material properties, and this phenomenon was accurately predicted by the simulation (Fig. 13(c)).

7.2.5. *Wrinkling during forming without a blank holder*

The hemispherical forming of a single layer without a blank holder was carried out. The yarn orientation was 0°/90° and the punch displacement was 75 mm. The geometry of the hemispherical punch and die mold can be seen in Fig. 12 and the fabric's final deformed shape is shown in Fig. 17a. The material used for the experiment was G1151® and the material properties are given in Table 2. The result of the simulation when using the presented stress resultant approach is shown in Fig. 17b, and it can be seen that the method gave rise to similar wrinkling in the plane area compared with the experimental results shown in Fig. 17a.

In order to carry out a more detailed comparison of the wrinkling shape between experiment and simulation, digital image correlation (DIC) experiments were conducted to obtain the forming shapes. This DIC experiment is shown in Fig. 17c, and through the two cameras used, the VIC-3D system calculated the position of the deformed fabric at the built coordinate system. The experimental result of the hemispherical forming without a blank holder is shown in Fig. 17d, where two paths (0° path and 45° path) are marked to highlight the comparison with the simulation. A comparison of the displacements in the direction of the Z axis of the two paths is shown in Fig. 17e and f, and as can be seen there was a fair agreement between experiment and simulation.

7.3. *Tetrahedral forming*

Tetrahedral forming has become a benchmark shape for woven reinforcement forming [34,64,91]. Fig. 18 shows the tetrahedral forming parameters: three layup configurations were considered, i.e., single layer of 0°/90°, single layer of ±45°, and four layers with a quasi-isotropic layup. For the single-layer forming, the final punch displacement was 90 mm, and for the four-layer forming, due to the distance limitations between the punch and die mold, the final punch displacement was set to 70 mm to form the tetrahedral part.

The final deformed experimental shapes are presented on the left side of Figs. 19 and 20. Fig. 19a shows the forming of a single layer of 0°/90° and Fig. 19b the forming of a single layer of ±45°. For the multilayer forming, with the help of the two cameras placed in the experimental setup (Fig. 11a), the bottom and top sides were captured to observe the different orientation angles of the fabric deformation. These can be seen in Fig. 20a and b and none of them presented any wrinkles.

Following this, simulations were carried out using the proposed stress resultant shell approach. Three node shell elements were used to mesh each single fabric layer. The forming simulations were carried out over half of the fabric, and 20,000 elements were used for each layer. The material used for the experiment was G1151®, and the material and friction properties used for the simulation were the same as for the hemispherical forming simulation (Table 2).

7.3.1. *In-plane shear angle comparison*

With the help of marker points on the fabric, a comparison was made between the in-plane shear angles obtained through experiment and simulation, and the results are shown on the right side of Figs. 19 and 20. The area with the larger shear angle was compared with the experiment, and both the bottom and top layers of the four-layer quasi-isotropic layup were compared with their experimentally obtained counterparts. As shown in Figs. 19 and 20, the presented approach could correctly predict the fabric's in-plane shear angle at different areas.

7.3.2. *Fabric contour comparison*

Comparisons of the fabric contour obtained by tetrahedral forming are shown in Fig. 21. It can be seen that the deformed fabric profile between experiment and simulation were similar.

8. Conclusion

The shell models to simulate the draping of fibrous reinforcements must take into account the specificity of the bending deformation due to the possible slippage between the fibers. The stress resultant shell approach proposed in this paper considers independent membrane and bending behaviors thus making it possible to take into account the low bending stiffness related to the fibrous constitution of textile reinforcements. The proposed hypoelastic behavior law cumulates the stress resultants in the frame of the fibers. The necessary experimental tests to identify the behavior in stress resultants during in-plane shear, bending and tension were presented. The proposed approach was validated by a set of forming processes for which the numerical simulation gave results in agreement with the forming experiments. The method was implemented in the ABAQUS software and can therefore be carried out by the users of this code as well as integrated in other finite element codes.

Nevertheless, it should be noted that the approach has a limitation. The stress resultant shell approach concerns the stress resultants and stress moments in terms of internal forces as well as the membrane strains and curvatures in terms of deformations. This does not explicitly give the distribution of strains and stresses according to the position in the thickness nor the rotation of material normals. The Kirchhoff hypothesis could be used to establish them from the mean surface determined by the stress resultant approach (curvatures and membrane strains). This was not relevant because it was shown that the material normals did not remain perpendicular to the mean surface during the deformation of the textile reinforcement and that the Kirchoff theory was therefore not valid. While the proposed approach is relevant for the calculation of mean surface deformations and for the simulation of wrinkles, an approach based on the physics of the deformation of fibrous reinforcements should be developed to determine the strains and the stresses through the thickness of the textile preform.

CRediT authorship contribution statement

Bo Chen: Investigation, Methodology, Software, Validation, Visualization, Writing - original draft. **Julien Colmars:** Investigation, Methodology, Supervision. **Naim Naouar:** Investigation, Software. **Philippe Boisse:** Conceptualization, Methodology, Supervision.

Declaration of Competing Interest

The authors declare that they have no known competing financial interests or personal relationships that could have appeared to influence the work reported in this paper.

Acknowledgements

This work was supported by the ANR, (French Research Agency), grant ANR-18-CE06-0011-04-AMOC and by the China Scholarship Council (CSC) (B. Chen).

References

[1] Šimáček P, Advani SG. Desirable features in mold filling simulations for liquid composite molding processes. Polym Compos 2004;25(4):355–67. https://doi.org/10.1002/pc.20029.
[2] Deléglise M, Le Grognec P, Binetruy C, Krawczak P, Claude B. Modeling of high speed RTM injection with highly reactive resin with on-line mixing. Compos Part A Appl Sci Manuf 2011;42:1390–7. https://doi.org/10.1016/j.compositesa.2011.06.002.
[3] Sozer EM, Simacek P, Advani SG. Resin transfer molding (RTM) in polymer matrix composites. Manuf. Tech. Polym. Matrix Compos. Elsevier; 2012. p. 245–309. https://doi.org/10.1533/9780857096258.3.243.
[4] Verrey J, Wakeman MD, Michaud V, Månson JAE. Manufacturing cost comparison of thermoplastic and thermoset RTM for an automotive floor pan. Compos Part A Appl Sci Manuf 2006;37:9–22. https://doi.org/10.1016/j.compositesa.2005.05.048.
[5] Lukaszewicz DHJA, Potter KD. The internal structure and conformation of prepreg with respect to reliable automated processing. Compos Part A Appl Sci Manuf 2011;42:283–92. https://doi.org/10.1016/j.compositesa.2010.11.014.
[6] Henning F, Kärger L, Dörr D, Schirmaier FJ, Seuffert J, Bernath A. Fast processing and continuous simulation of automotive structural composite components. Compos Sci Technol 2019;171:261–79. https://doi.org/10.1016/j.compscitech.2018.12.007.
[7] Gong Y, Xu P, Peng X, Wei R, Yao Y, Zhao K. A lamination model for forming simulation of woven fabric reinforced thermoplastic prepregs. Compos Struct 2018;196:89–95. https://doi.org/10.1016/J.COMPSTRUCT.2018.05.004.
[8] Gereke T, Döbrich O, Hübner M, Cherif C. Experimental and computational composite textile reinforcement forming: a review. Compos Part A Appl Sci Manuf 2013;46:1–10. https://doi.org/10.1016/j.compositesa.2012.10.004.
[9] Boisse P, Hamila N, Madeo A. The difficulties in modeling the mechanical behavior of textile composite reinforcements with standard continuum mechanics of Cauchy. Some possible remedies. Int J Solids Struct 2018;154:55–65. https://doi.org/10.1016/j.ijsolstr.2016.12.019.
[10] Durville D. Simulation of the mechanical behaviour of woven fabrics at the scale of fibers. Int J Mater Form 2010;3:1241–51. https://doi.org/10.1007/s12289-009-0674-7.
[11] Latil P, Orgéas L, Geindreau C, Dumont PJJ, Rolland du Roscoat S. Towards the 3D in situ characterisation of deformation micro-mechanisms within a compressed bundle of fibres. Compos Sci Technol 2011;71:480–8. https://doi.org/10.1016/j.compscitech.2010.12.023.
[12] El Said B, Ivanov D, Long AC, Hallett SR. Multi-scale modelling of strongly heterogeneous 3D composite structures using spatial Voronoi tessellation. J Mech Phys Solids 2016;88:50–71. https://doi.org/10.1016/j.jmps.2015.12.024.
[13] Daelemans L, Faes J, Allaoui S, Hivet G, Dierick M, Van Hoorebeke L, et al. Finite element simulation of the woven geometry and mechanical behaviour of a 3D woven dry fabric under tensile and shear loading using the digital element method. Compos Sci Technol 2016;137:177–87. https://doi.org/10.1016/j.compscitech.2016.11.003.
[14] Yousaf Z, Potluri P, Withers PJ, Mollenhauer D, Zhou E, Duning S. Digital element simulation of aligned tows during compaction validated by computed tomography (CT). Int J Solids Struct 2018;154:78–87. https://doi.org/10.1016/j.ijsolstr.2017.05.044.
[15] Skordos AA, Monroy Aceves C, Sutcliffe MPF. A simplified rate dependent model of forming and wrinkling of pre-impregnated woven composites. Compos Part A Appl Sci Manuf 2007;38:1318–30. https://doi.org/10.1016/j.compositesa.2006.11.005.
[16] Potter K, Khan B, Wisnom M, Bell T, Stevens J. Variability, fibre waviness and misalignment in the determination of the properties of composite materials and structures. Compos Part A Appl Sci Manuf 2008;39:1343–54. https://doi.org/10.1016/j.compositesa.2008.04.016.
[17] Boisse P, Hamila N, Vidal-Sallé E, Dumont F. Simulation of wrinkling during textile composite reinforcement forming. Influence of tensile, in-plane shear and bending

stiffnesses. Compos Sci Technol 2011;71:683–92. https://doi.org/10.1016/j.compscitech.2011.01.011.
[18] Belnoue JP-H, Nixon-Pearson OJ, Thompson AJ, Ivanov DS, Potter KD, Hallett SR. Consolidation-driven defect generation in thick composite parts. J Manuf Sci Eng 2018;140. https://doi.org/10.1115/1.4039555.
[19] Simo JC, Fox DD. On a stress resultant geometrically exact shell model. Part I: Formulation and optimal parametrization. Comput Methods Appl Mech Eng 1989;72:267–304. https://doi.org/10.1016/0045-7825(89)90002-9.
[20] Ibrahimbegović A. Stress resultant geometrically nonlinear shell theory with drilling rotations-Part I. A consistent formulation. Comput Methods Appl Mech Eng 1994;118:265–84. https://doi.org/10.1016/0045-7825(94)90003-5.
[21] Yang HTY, Saigal S, Masud A, Kapania RK. A survey of recent shell finite elements. Int J Numer Methods Eng 2000;47:101–27. https://doi.org/10.1002/(SICI)1097-0207(20000110/30)47:1/3<101::AID-NME763>3.0.CO;2-C.
[22] Onate E, Zienkiewicz OC. A viscous shell formulation for the analysis of thin sheet metal forming. Int J Mech Sci 1983;25:305–35. https://doi.org/10.1016/0020-7403(83)90011-5.
[23] Bergman G, Oldenburg M. A finite element model for thermomechanical analysis of sheet metal forming. Int J Numer Methods Eng 2004;59:1167–86. https://doi.org/10.1002/nme.911.
[24] Gelin JC, Cherouat A, Boisse P, Sabhi H. Manufacture of thin composite structure by the RTM process: Numerical simulation of the shaping operation. Compos Sci Technol 1996;56:711–8. https://doi.org/10.1016/0266-3538(96)00011-5.
[25] Cherouat A, Billoët JL. Mechanical and numerical modelling of composite manufacturing processes deep-drawing and laying-up of thin pre-impregnated woven fabrics. J Mater Process Technol 2001;118:460–71. https://doi.org/10.1016/S0924-0136(01)00987-6.
[26] Cao J, Xue P, Peng X, Krishnan N. An approach in modeling the temperature effect in thermo-stamping of woven composites. Compos Struct 2003;61:413–20. https://doi.org/10.1016/S0263-8223(03)00052-7.
[27] Yu WR, Zampaloni M, Pourboghrat F, Chung K, Kang TJ. Analysis of flexible bending behavior of woven preform using non-orthogonal constitutive equation. Compos Part A Appl Sci Manuf 2005;36:839–50. https://doi.org/10.1016/j.compositesa.2004.10.026.
[28] ten Thije RHW, Akkerman R, Huétink J. Large deformation simulation of anisotropic material using an updated Lagrangian finite element method. Comput Methods Appl Mech Eng 2007;196:3141–50. https://doi.org/10.1016/j.cma.2007.02.010.
[29] Lin H, Wang J, Long AC, Clifford MJ, Harrison P. Predictive modelling for optimization of textile composite forming. Compos Sci Technol 2007;67:3242–52. https://doi.org/10.1016/j.compscitech.2007.03.040.
[30] Chen S, Harper LT, Endruweit A, Warrior NA. Formability optimisation of fabric preforms by controlling material draw-in through in-plane constraints. Compos Part A Appl Sci Manuf 2015;76:10–9. https://doi.org/10.1016/j.compositesa.2015.05.006.
[31] Döbrich O, Gereke T, Diestel O, Krzywinski S, Cherif C. Decoupling the bending behavior and the membrane properties of finite shell elements for a correct description of the mechanical behavior of textiles with a laminate formulation. J Ind Text 2013;44:70–84. https://doi.org/10.1177/1528083713477442.
[32] Dangora LM, Mitchell CJ, Sherwood JA. Predictive model for the detection of out-of-plane defects formed during textile-composite manufacture. Compos Part A Appl Sci Manuf 2015;78:102–12. https://doi.org/10.1016/j.compositesa.2015.07.011.
[33] Boisse P, Colmars J, Hamila N, Naouar N, Steer Q. Bending and wrinkling of composite fiber preforms and prepregs. A review and new developments in the draping simulations. Compos Part B Eng 2018;141:234–49. https://doi.org/10.1016/j.compositesb.2017.12.061.
[34] Thompson AJ, Belnoue JP-H, Hallett SR. Modelling defect formation in textiles during the double diaphragm forming process. Compos Part B Eng 2020;202:108357. https://doi.org/10.1016/j.compositesb.2020.108357.
[35] Mathieu S, Hamila N, Bouillon F, Boisse P. Enhanced modeling of 3D composite preform deformations taking into account local fiber bending stiffness. Compos Sci Technol 2015;117:322–33. https://doi.org/10.1016/j.compscitech.2015.07.005.
[36] Nishii M, Hirashima T, Kurashiki T. Dry fabric forming analysis considering the influence of tensions on in-plane shear behavior. J Soc Mater Sci Japan 2014;63:380–5. https://doi.org/10.2472/jsms.63.380.
[37] Jauffrès D, Sherwood JA, Morris CD, Chen J. Discrete mesoscopic modeling for the simulation of woven-fabric reinforcement forming. Int J Mater Form 2010;3:1205–16. https://doi.org/10.1007/s12289-009-0646-y.
[38] Harrison P, Gomes R, Curado-Correia N. Press forming a 0/90 cross-ply advanced thermoplastic composite using the double-dome benchmark geometry. Compos Part A Appl Sci Manuf 2013;54:56–69. https://doi.org/10.1016/j.compositesa.2013.06.014.
[39] Mitchell CJ, Dangora LM, Sherwood JA. Investigation into a robust finite element model for composite materials. Finite Elem Anal Des 2016;115:1–8. https://doi.org/10.1016/j.finel.2016.02.003.
[40] Giorgio I, Harrison P, dell'Isola F, Alsayednoor J, Turco E. Wrinkling in engineering fabrics: a comparison between two different comprehensive modelling approaches. Proceedings Math Phys Eng Sci 2018;474:20180063. https://doi.org/10.1098/rspa.2018.0063.
[41] Haanappel SP, Ten Thije RHW, Sachs U, Rietman B, Akkerman R. Formability analyses of uni-directional and textile reinforced thermoplastics. Compos Part A Appl Sci Manuf 2014;56:80–92. https://doi.org/10.1016/j.compositesa.2013.09.009.
[42] Dörr D, Schirmaier FJ, Henning F, Kärger L. A viscoelastic approach for modeling bending behavior in finite element forming simulation of continuously fiber reinforced composites. Compos Part A Appl Sci Manuf 2017;94:113–23. https://doi.org/10.1016/j.compositesa.2016.11.027.
[43] Dörr D, Henning F, Kärger L. Nonlinear hyperviscoelastic modelling of intra-ply deformation behaviour in finite element forming simulation of continuously fibre-reinforced thermoplastics. Compos Part A Appl Sci Manuf 2018;109:585–96. https://doi.org/10.1016/j.compositesa.2018.03.037.
[44] Ahmad S, Irons BM, Zienkiewicz OC. Analysis of thick and thin shell structures by curved finite elements. Int J Numer Methods Eng 1970;2:419–51. https://doi.org/10.1002/nme.1620020310.
[45] Dvorkin EN, Bathe K. A continuum mechanics based four-node shell element for general non-linear analysis. Eng Comput 1984;1:77–88. https://doi.org/10.1108/eb023562.
[46] Parisch H. A continuum-based shell theory for non-linear applications. Int J Numer Methods Eng 1995;38:1855–83. https://doi.org/10.1002/nme.1620381105.
[47] Hamila N, Boisse P, Sabourin F, Brunet M. A semi-discrete shell finite element for textile composite reinforcement forming simulation. Int J Numer Meth Eng 2009;79:1443–66. https://doi.org/10.1002/nme.2625.
[48] Hughes TJR, Winget J. Finite rotation effects in numerical integration of rate constitutive equations arising in large-deformation analysis. Int J Numer Methods Eng 1980;15:1862–7. https://doi.org/10.1002/nme.1620151210.
[49] Xiao H, Bruhns OT, Meyers A. Hypo-elasticity model based upon the logarithmic stress rate. J Elast 1997;47:51–68. https://doi.org/10.1023/A:1007356925912.
[50] Belytschko T, Liu WK, Moran B, Elkhodary K. Nonlinear finite elements for continua and structures. John wiley & sons; 2013.
[51] Peng XQ, Cao J. A continuum mechanics-based non-orthogonal constitutive model for woven composite fabrics. Compos Part A Appl Sci Manuf 2005;36:859–74. https://doi.org/10.1016/j.compositesa.2004.08.008.
[52] Khan MA, Mabrouki T, Gauthier S, Vidal-Salle E, Boisse P. Preforming simulation of the reinforcements of woven composites: continuous approach within a commercial code. Int J Mater Form 2008;1:879–82. https://doi.org/10.1007/s12289-008-0236-4.
[53] Khan MA, Mabrouki T, Vidal-Sallé E, Boisse P. Numerical and experimental analyses of woven composite reinforcement forming using a hypoelastic behaviour. Application to the double dome benchmark. J Mater Process Technol 2010;210:378–88. https://doi.org/10.1016/j.jmatprotec.2009.09.027.
[54] Nasri M, Garnier C, Abbassi F, Labanieh AR, Dalverny O, Zghal A. Hybrid approach for woven fabric modelling based on discrete hypoelastic behaviour and experimental validation. Compos Struct 2019;209:992–1004. https://doi.org/10.1016/j.compstruct.2018.10.081.
[55] Khan MA, Saleem W, Asad M, Ijaz H. A parametric sensitivity study on preforming simulations of woven composites using a hypoelastic computational model. J Reinf Plast Compos 2015;35:243–57. https://doi.org/10.1177/0731684415613567.
[56] Charmetant A, Orliac JG, Vidal-Sallé E, Boisse P. Hyperelastic model for large deformation analyses of 3D interlock composite preforms. Compos Sci Technol 2012;72:1352–60. https://doi.org/10.1016/J.COMPSCITECH.2012.05.006.
[57] Peng X, Guo Z, Du T, Yu WR. A simple anisotropic hyperelastic constitutive model for textile fabrics with application to forming simulation. Compos Part B Eng 2013;52:275–81. https://doi.org/10.1016/j.compositesb.2013.04.014.
[58] Yin H, Peng X, Du T, Guo Z. Draping of plain woven carbon fabrics over a double-curvature mold. Compos Sci Technol 2014;92:64–9. https://doi.org/10.1016/j.compscitech.2013.12.013.
[59] Gong Y, Peng X, Yao Y, Guo Z. An anisotropic hyperelastic constitutive model for thermoplastic woven composite prepregs. Compos Sci Technol 2016;128:17–24. https://doi.org/10.1016/j.compscitech.2016.03.005.
[60] Dafalias YF. Corotational rates for kinematic hardening at large plastic deformations. J Appl Mech 1983;50:561–5. https://doi.org/10.1115/1.3167091.
[61] Dienes JK. On the analysis of rotation and stress rate in deforming bodies. Acta Mech 1979;32:217–32. https://doi.org/10.1007/BF01379008.
[62] Boisse P, Gasser A, Hagege B, Billoet J-L. Analysis of the mechanical behavior of woven fibrous material using virtual tests at the unit cell level. J Mater Sci 2005;40:5955–62. https://doi.org/10.1007/s10853-005-5069-7.
[63] Badel P, Vidal-Sallé E, Boisse P. Large deformation analysis of fibrous materials using rate constitutive equations. Comput Struct 2008;86:1164–75. https://doi.org/10.1016/j.compstruc.2008.01.009.
[64] Allaoui S, Boisse P, Chatel S, Hamila N, Hivet G, Soulat D, et al. Experimental and numerical analyses of textile reinforcement forming of a tetrahedral shape. Compos Part A Appl Sci Manuf 2011;42:612–22. https://doi.org/10.1016/j.compositesa.2011.02.001.
[65] Gherissi A, Abbassi F, Ammar A, Zghal A. Numerical and experimental investigations on deep drawing of G1151 carbon fiber woven composites. Appl Compos Mater 2016;23:461–76. https://doi.org/10.1007/s10443-015-9468-x.
[66] Badel P, Vidal-Sallé E, Maire E, Boisse P. Simulation and tomography analysis of textile composite reinforcement deformation at the mesoscopic scale. Compos Sci Technol 2008;68:2433–40. https://doi.org/10.1016/j.compscitech.2008.04.038.
[67] Lebrun G, Bureau MN, Denault J. Evaluation of bias-extension and picture-frame test methods for the measurement of intraply shear properties of PP/glass commingled fabrics. Compos Struct 2003;61:341–52. https://doi.org/10.1016/S0263-8223(03)00057-6.
[68] Harrison P, Clifford MJ, Long AC. Shear characterisation of viscous woven textile composites: a comparison between picture frame and bias extension experiments. Compos Sci Technol 2004;64:1453–65. https://doi.org/10.1016/j.compscitech.2003.10.015.
[69] Launay J, Hivet G, Duong AV, Boisse P. Experimental analysis of the influence of tensions on in plane shear behaviour of woven composite reinforcements. Compos Sci Technol 2008;68:506–15. https://doi.org/10.1016/j.compscitech.2007.06.021.

[70] Cao J, Akkerman R, Boisse P, Chen J, Cheng HS, de Graaf EF, et al. Characterization of mechanical behavior of woven fabrics: experimental methods and benchmark results. Compos Part A Appl Sci Manuf 2008;39:1037–53. https://doi.org/10.1016/j.compositesa.2008.02.016.
[71] Lomov SV, Willems A, Verpoest I, Zhu Y, Barburski M, Stoilova T. Picture frame test of woven composite reinforcements with a full-field strain registration. Text Res J 2006;76:243–52. https://doi.org/10.1177/0040517506061032.
[72] Hosseini A, Kashani MH, Sassani F, Milani AS, Ko FK. Identifying the distinct shear wrinkling behavior of woven composite preforms under bias extension and picture frame tests. Compos Struct 2018;185:764–73. https://doi.org/10.1016/j.compstruct.2017.11.033.
[73] Bel S, Boisse P, Dumont F. Analyses of the deformation mechanisms of non-crimp fabric composite reinforcements during preforming. Appl Compos Mater 2012;19:513–28. https://doi.org/10.1007/s10443-011-9207-x.
[74] ASTM. Standard test method for stiffness of fabrics; 2002. https://doi.org/10.1520/D1388-96R02.
[75] de Bilbao E, Soulat D, Hivet G, Gasser A. Experimental study of bending behaviour of reinforcements. Exp Mech 2010;50:333–51. https://doi.org/10.1007/s11340-009-9234-9.
[76] Syerko E, Comas-Cardona S, Binetruy C. Models of mechanical properties/behavior of dry fibrous materials at various scales in bending and tension: a review. Compos Part A Appl Sci Manuf 2012;43:1365–88. https://doi.org/10.1016/j.compositesa.2012.03.012.
[77] Lammens N, Kersemans M, Luyckx G, Van Paepegem W, Degrieck J. Improved accuracy in the determination of flexural rigidity of textile fabrics by the Peirce cantilever test (ASTM D1388). Text Res J 2014;84:1307–14. https://doi.org/10.1177/0040517514523182.
[78] Sachs U, Akkerman R. Viscoelastic bending model for continuous fiber-reinforced thermoplastic composites in melt. Compos Part A Appl Sci Manuf 2017;100:333–41. https://doi.org/10.1016/j.compositesa.2017.05.032.
[79] Alshahrani H, Hojjati M. A new test method for the characterization of the bending behavior of textile prepregs. Compos Part A Appl Sci Manuf 2017;97:128–40. https://doi.org/10.1016/j.compositesa.2017.02.027.
[80] Liang B, Chaudet P, Boisse P. Curvature determination in the bending test of continuous fibre reinforcements. Strain 2017;53:e12213. https://doi.org/10.1111/str.12213.
[81] Kawabata S, Niwa M, Kawai H. The finite deformation theory of plain weave fabrics. Part I: the biaxial deformation theory. J Text Inst 1973;64:21–46. https://doi.org/10.1080/00405007308630416.
[82] Buet-Gautier K, Boisse P. Experimental analysis and modeling of biaxial mechanical behavior of woven composite reinforcements. Exp Mech 2001;41:260–9. https://doi.org/10.1007/BF02323143.
[83] Willems A, Lomov SV, Verpoest I, Vandepitte D. Optical strain fields in shear and tensile testing of textile reinforcements. Compos Sci Technol 2008;68:807–19. https://doi.org/10.1016/j.compscitech.2007.08.018.
[84] Carvelli V, Corazza C, Poggi C. Mechanical modelling of monofilament technical textiles. Comput Mater Sci 2008;42:679–91. https://doi.org/10.1016/j.commatsci.2007.10.003.
[85] Harrison P, Abdiwi F, Guo Z, Potluri P, Yu WR. Characterising the shear-tension coupling and wrinkling behaviour of woven engineering fabrics. Compos Part A Appl Sci Manuf 2012;43:903–14. https://doi.org/10.1016/j.compositesa.2012.01.024.
[86] Nosrat-Nezami F, Gereke T, Eberdt C, Cherif C. Characterisation of the shear-tension coupling of carbon-fibre fabric under controlled membrane tensions for precise simulative predictions of industrial preforming processes. Compos Part A Appl Sci Manuf 2014;67:131–9. https://doi.org/10.1016/j.compositesa.2014.08.030.
[87] Komeili M, Milani AS. On effect of shear-tension coupling in forming simulation of woven fabric reinforcements. Compos Part B Eng 2016;99:17–29. https://doi.org/10.1016/j.compositesb.2016.05.004.
[88] Yao Y, Peng X, Gong Y. Influence of tension–shear coupling on draping of plain weave fabrics. J Mater Sci 2019;54:6310–22. https://doi.org/10.1007/s10853-019-03334-w.
[89] Alshahrani H. Characterization and finite element modeling of coupled properties during polymer composites forming processes. Mech Mater 2020;144:103370. https://doi.org/10.1016/j.mechmat.2020.103370.
[90] Guzman-Maldonado E, Wang P, Hamila N, Boisse P. Experimental and numerical analysis of wrinkling during forming of multi-layered textile composites. Compos Struct 2019;208:213–23. https://doi.org/10.1016/j.compstruct.2018.10.018.
[91] Allaoui S, Hivet G, Soulat D, Wendling A, Ouagne P, Chatel S. Experimental preforming of highly double curved shapes with a case corner using an interlock reinforcement. Int J Mater Form 2014;7:155–65. https://doi.org/10.1007/s12289-012-1116-5.